



Quinazoline-Glycine Manganese(II) Nano-Complex for Arsenic Sensing via QCM: Synthesis, Characterization, DFT Studies, Biological Evaluation and Environmental Application



M. S. A. Mansour^{1*}, Abeer T. Abd-Elkarim¹, Walaa H. Mahmoud¹, Ahmed A. El-Sherif¹

¹Chemistry Department, Faculty of Science, Cairo University, Giza, 12613 Egypt

Abstract

Arsenic is a toxic metalloid that occurs naturally in the Earth's crust. Its widespread distribution and mobility have led to extensive environmental contamination and adverse human health effects across numerous regions worldwide. Monitoring arsenic concentrations in ecosystems is crucial for mitigating potential hazards and minimizing human exposure. This research outlines the synthesis, characterization, and application of an innovative Schiff base Quinazoline ligand and its corresponding ternary Mn(II) complex for arsenic sensing. A manganese (II) coordination compound featuring a principal ligand denoted (WMS) and an auxiliary ligand Glycine (GLY) was synthesized and comprehensively characterized using analytical techniques such as FT-IR, UV-Vis, mass spectrometry, elemental analysis, and electrical conductance measurements. Thermal analysis (TGA) of the Manganese (II) complex corroborated well with the proposed formula derived from the analytical data. The molecular formula of the complex was determined to be $[\text{Mn}(\text{WMS})(\text{Gly})\text{H}_2\text{O}] \cdot \text{Cl} \cdot \text{H}_2\text{O}$, with the (WMS) ligand exhibiting tridentate chelation behavior by coordinating with the central Mn(II) ion through its two azomethine nitrogen atoms and one pyridine nitrogen. The (Gly) ligand bound to Mn (II) via deprotonated carboxylate oxygen and the (NH₂) nitrogen, resulting in a distorted Octahedral geometry. In addition, Density Functional Theory (DFT) calculations are performed to determine the optimal structure of the Schiff base (WMS) and its Mn (II) complex. The HOMO-LUMO energy gaps, chemical hardness, and dipole moments of the (WMS) and its Manganese complex were also investigated. The study examined the biological roles of the (WMS) and its Mn (II) complex, specifically focusing on its antibacterial, antifungal, and anticancer properties. To understand the molecular interactions, we conducted molecular docking simulations to determine the potential binding orientations of the (WMS) and its Mn (II) complex with active sites on the receptor (3HB5). The docking analyses were conducted meticulously utilizing the MOE program, renowned for its robust, stiff molecular docking capabilities. Extensive characterization of the nano-sized Quinazoline Manganese complex involved dynamic light scattering (DLS), zeta potential analysis, x-ray diffraction (XRD), atomic force microscopy (AFM), BET surface area determination, and pore size analysis. The possible application of this nano-complex as a quartz crystal microbalance (QCM) sensor for detecting arsenic contamination in water was investigated. The sensor exhibited rapid response times (less than 2 minutes), excellent mechanical stability (confirmed by contact angle measurements), and consistent performance across varying pH and temperature conditions. This research highlights the synthesis of new arsenic-sensing material and its promising application in continuous environmental monitoring. Given the widespread prevalence of arsenic contamination, particularly in groundwater sources used for drinking and irrigation, developing sensitive and selective arsenic sensors is paramount for safeguarding public health and ecosystem integrity.

Keywords : Arsenic ; Nanoparticles; QCM sensor; DFT; Docking; Schiff base; Manganese

1. Introduction

Arsenic, a ubiquitous metalloid, has emerged as a significant environmental concern, posing severe threats to human health and ecological systems worldwide. Its natural occurrence in the Earth's crust and anthropogenic activities have led to widespread contamination, particularly in groundwater sources used for drinking and irrigation [1,2]. The adverse effects of arsenic exposure range from acute toxicity to chronic diseases, including various cancers, cardiovascular disorders, and neurological deficits [3,4]. Consequently, developing sensitive and selective arsenic detection methods has become a priority for safeguarding public health and preserving ecosystem integrity [5, 6]. Schiff base complexes, derived from the condensation of primary amines and carbonyl compounds, have garnered substantial interest in various fields due to their remarkable structural diversity and potential applications [7-9]. These complexes, particularly those incorporating transition metals and mixed ligands, have demonstrated promising properties for sensing, catalysis, and biological activities [10, 11]. The rational design and synthesis of Schiff base complexes with tailored properties have opened new avenues for addressing critical environmental and health-related challenges. Incorporating transition metals into Schiff base complexes has yielded fascinating molecular architectures with unique electronic and structural features [12]. The judicious selection of metal ions and their coordination environments can modulate these complexes' physicochemical properties and reactivity, enabling various applications. Furthermore, incorporating mixed ligands, such as amino acids like glycine, can introduce additional functionalities and enhance the complexes' performance in specific applications [13]. Computational chemistry techniques,

*Corresponding author e-mail: Adammidomansour@gmail.com, (PhD Candidate Student).

Receive Date: 02 June 2024, Revise Date: 26 June 2024, Accept Date: 01 July 2024

DOI: 10.21608/ejchem.2024.294794.9796

©2025 National Information and Documentation Center (NIDOC)

particularly Density Functional Theory (DFT), have emerged as powerful tools for elucidating Schiff base complexes' structural, electronic, and reactivity properties [14-16]. DFT calculations provide valuable insights into these complexes' optimal geometries, charge distributions, and energy levels, facilitating the rational design of new materials [15, 16]. Mixed-ligand transition metal complexes, including those derived from Schiff bases, have demonstrated remarkable biological activities, such as antimicrobial, antifungal, and anticancer properties [17, 18]. The synergistic effects of the metal center, Schiff base ligand, and auxiliary ligands contribute to their potent bioactivities, making them attractive candidates for therapeutic applications [19, 20]. Exploring the biological potential of these complexes can lead to the development of new and effective treatments for various diseases. Molecular docking simulations have emerged as a powerful computational technique for understanding the molecular interactions between potential drug candidates and their target receptors [21]. By predicting the binding orientations and affinities of Schiff base complexes with specific biological targets, molecular docking can provide valuable insights into their potential bioactivities and guide the design of more potent and selective compounds [22, 23]. Integrating Schiff base complexes with nanoparticles has gained significant attention due to nanomaterials' unique properties and enhanced performance [24, 25]. Nanoparticles exhibit a high surface-to-volume ratio, which can lead to improved reactivity, catalytic activity, and sensing capabilities [26, 27]. Additionally, the nanoscale size of these materials can facilitate their integration into various sensing platforms, enabling the development of miniaturized and highly sensitive detection systems [28]. The combination of Schiff base complexes and nanoparticles has shown promising results in various applications, including sensing, catalysis, and biomedical fields [29, 30]. Integrating nano-sized Schiff base complexes with quartz crystal microbalance (QCM) sensors has shown promising results for detecting various analytes, including arsenic [31, 32]. QCM sensors offer high sensitivity, rapid response times, and the ability to operate in real-time, making them ideal for continuous environmental monitoring [33, 34]. Incorporating nano-complexes with tailored properties can enhance the selectivity and sensitivity of these sensors, enabling accurate detection of arsenic contamination in water sources [34]. This study presents the synthesis, characterization, and application of an innovative Schiff base quinazoline ligand and its corresponding ternary Mn(II) complex for arsenic sensing. The complex, featuring a mixed-ligand system comprising the principal ligand (**WMS**) and the auxiliary ligand glycine (**Gly**), was comprehensively characterized using various analytical techniques. Density Functional Theory (DFT) calculations were performed to elucidate the complex's optimal structure, electronic properties, and chemical reactivity. Furthermore, the biological activities of the complex, including antibacterial, antifungal, and anticancer properties, were evaluated, highlighting its potential therapeutic applications. Molecular docking simulations were conducted to gain insights into the binding interactions between the Schiff base complex and a specific biological target receptor (**3HB5**) [35, 36]. The integration of the nano-sized quinazoline manganese complex with a quartz crystal microbalance (QCM) sensor was explored for the selective detection of arsenic contamination in water sources. The sensor exhibited rapid response times, excellent mechanical stability, and consistent performance across varying environmental conditions, showcasing its potential for continuous environmental monitoring. By combining experimental and computational approaches, this study aims to contribute to developing sensitive and selective arsenic sensing materials while exploring their biological activities and potential therapeutic applications. Addressing the global challenge of arsenic contamination through innovative materials and sensing technologies is crucial for safeguarding public health and preserving the integrity of our ecosystems.

2. Experimental part.

2.1. Experimental Procedures and Methodology.

In this research, chemicals of high purity were utilized, including 4-hydrazineylquinazoline 98% and (E)-1-(2-(p-tolyl)hydrazineylidene)propan-2-one 99% (sourced from Merck), glycine $\geq 99\%$ and Manganese(II) chloride tetrahydrate $\geq 99\%$ ($\text{MnCl}_2 \cdot 4\text{H}_2\text{O}$) (procured from BDH). Absolute Ethanol (Ethyl alcohol 99.9%), an organic solvent of spectroscopic purity, was sourced from BDH. For all preparations, bidistilled water obtained from glass equipment was consistently used. The human tumor cell line, MCF-7, stored in liquid nitrogen at -180°C , was obtained from the American Type Culture Collection. Cultivation and maintenance of the MCF-7 tumor cell line were conducted at the National Cancer Institute in Cairo, Egypt, through serial sub-culturing.

2.1.1. Solutions

Reservoir solutions containing the Schiff base ligand (**WMS**), glycine, and their corresponding metal complex, each formulated at a specific concentration of 1×10^{-3} M, were created by precisely dissolving the appropriate weight in ethanol for Schiff base ligand (**WMS**), glycine (**Gly**), and Mn (II) complex. The conductivity of the 1×10^{-3} M metal complex solution was then measured. Subsequently, solutions of the (**WMS**) and its ternary Mn (II) complex were diluted to a concentration of 1×10^{-4} M, utilizing precise dilution techniques from the initially prepared reservoir solutions for UV-Vis spectra measurement.

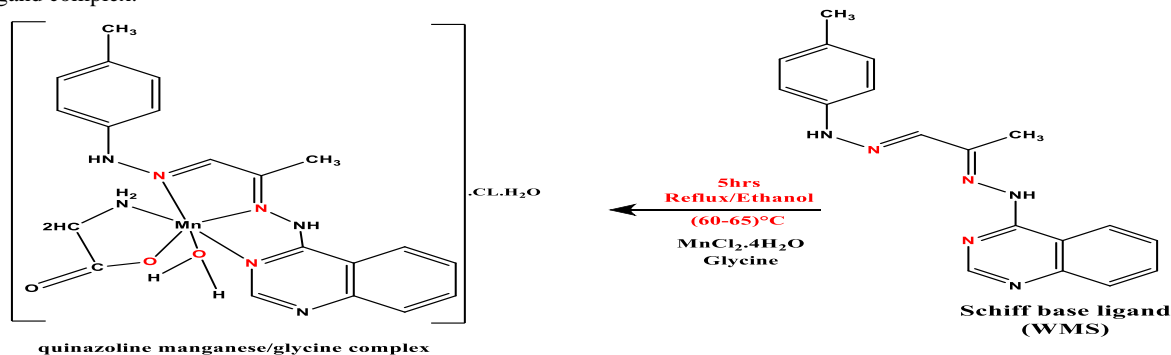
2.2. Instrumentation

Various analytical instruments and techniques were employed to characterize materials and investigate their properties. The CHNS-932 elemental analyzer was utilized to determine the carbon, hydrogen, and nitrogen content. Melting points were assessed using the triforme XMTD-3000 apparatus. Fourier transform infrared (FT-IR) spectra were generated using a Perkin-Elmer 1650 spectrometer with KBr disks. The molar conductance of complex solutions in DMSO was measured using a Jenway 4010 conductivity meter. Mass spectra were obtained via electron ionization at 70 eV on an MS-5988 mass spectrometer. UV-Vis absorption spectra were recorded using a Perkin-Elmer spectrophotometer. Antimicrobial studies were conducted at the Microanalytical Center, while cytotoxicity testing occurred at the National Cancer Institute and Cairo University. To characterize the nano-sized quinazoline manganese complex, particle size and surface charge were analyzed using a Nano Sight NS500. After sample degassing, BET surface area and pore volume were determined with a Nova Touch

4L surface area and pore volume analyzer. High-resolution AFM with an Oxford Jupiter XR was used to examine morphology. The nano-sized complex underwent sonication before AFM imaging. Thin films were synthesized via spin coating with a Laurell-650Sz coater under vacuum, and AFM was employed to image the films and measure roughness using a gold-tipped probe. Wettability was assessed using the sessile drop method with a Biolin Scientific T200 contact angle analyzer. QCM Nano sensors were fabricated by attaching the nano-sized quinazoline manganese complex to gold electrode quartz chips, with gold cleaning and baseline measurements taken before nanoparticle immobilization (Fig 1). The nano-sized quinazoline manganese complex has flowed over the sensors at a controlled rate.

2.3. Synthesis of Quinazoline Manganese Complex and its Nano Form

It built upon previous work synthesizing new quinazoline Schiff base (Scheme 1) [11, 37]. For synthesizing the mixed ligand quinazoline manganese complex, the synthesized quinazoline Schiff base ligand (**WMS**), the principal ligand, was formulated by dissolving (0.314 mmol, 0.10 g) in 40 mL of heated absolute ethanol. The secondary ligand amino acid glycine (Gly) (0.314 mmol, 0.02 g) was solubilized in 10 mL of heated distilled water. The chelate was formed by combining the hot solution of the principal quinazoline ligand (**WMS**) in absolute ethanol with the secondary glycine ligand in distilled water. A hot ethanolic solution (20 mL) of the metal salt $MnCl_2 \cdot 4H_2O$ (0.314 mmol) was gradually added dropwise. The resultant solution underwent reflux for Five hours, forming a precipitate representing the mixed ligand complex. This precipitate was collected by filtration and further purified through multiple washes using a combination of ethanol and water. Subsequently, it was desiccated under vacuum using anhydrous $CaCl_2$. Additionally, the synthesized quinazoline manganese/glycine complex underwent 10 minutes of ultrasonic probe treatment to convert it to the nanoscale form, resulting in a distinct color change (Change from dark brown to reddish brown) [11, 31, 33]. Scheme 1 illustrates the structure and formation reaction of the mixed ligand complex.



Scheme 1. Synthesis and Structural Representation of the Quinazoline Schiff Base Ligand (**WMS**) and Its Mixed Ligand Manganese Complex with Glycine

2.4. Computational Studies

Density functional theory (DFT) calculations [38] were performed on the quinazoline ligand (**WMS**) and its manganese (II) complex using the DMOL3 program [39, 40] within the Materials Studio software [39, 40]. This implements large-scale DFT with double numerical plus polarization (DNP) basis sets, which are more accurate than equivalent-sized 6-31G Gaussian basis sets [41-43]. The geometries were optimized without symmetry restrictions using the GGA-RPBE functional, which provides good correlation performance [44]. Key quantum chemical parameters were computed, such as the highest occupied molecular orbital energy (E_{HOMO}), lowest unoccupied molecular orbital energy (E_{LUMO}), and the HOMO-LUMO energy gap (ΔE). These calculations provided insights into the electronic properties and chemical reactivity of the quinazoline ligand (**WMS**) and its manganese (II) complex.

2.5. Biological Evaluation

2.5.1. Antimicrobial Activity Assessment

2.5.1.1. Antimicrobial Susceptibility Testing:

The antimicrobial potential of the synthesized quinazoline ligand (**WMS**) and its manganese (II) complex was investigated using the agar well diffusion method [45]. The compounds were evaluated for their antibacterial activity against Gram-positive bacteria, including *Staphylococcus aureus* (ATCC:13565), and *Streptococcus mutans* (ATCC:25175), as well as Gram-negative bacteria, such as *Escherichia coli* (ATCC:10536), and *Klebsiella pneumonia* (ATCC:10031). The antifungal activity was assessed against *Candida albicans* and *Aspergillus niger* using Sabouraud dextrose agar medium. Ampicillin and gentamicin were employed as reference antibacterial agents for Gram-positive and Gram-negative bacteria, respectively, while nystatin served as the standard antifungal drug [46]. Dimethyl sulfoxide (DMSO) was used as the solvent control. The compounds were tested at a 15 mg/mL concentration against bacterial and fungal strains. This experimental setup facilitated the evaluation of the antimicrobial efficacy of the quinazoline ligand and its manganese complex against a diverse range of clinically relevant microorganisms, encompassing Gram-positive and Gram-negative bacteria, as well as fungal species, including standard antimicrobial drugs, allowing for comparative analysis of the compounds' activities related.

2.5.1.2. Antimicrobial Susceptibility Testing Procedure:

The assessment of the antimicrobial potential of the quinazoline ligand (WMS) and its manganese (II) complex followed a standardized methodology. Sterilized media were aseptically poured into sterile Petri dishes and allowed to solidify at ambient temperature. Microbial suspensions were carefully prepared in sterile saline solution, with the turbidity adjusted to match the McFarland 0.5 standard, corresponding to a concentration of 1.5×10^5 CFU/mL. The turbidity was precisely calibrated to an optical density of 0.13 at a wavelength of 625 nm using a spectrophotometer [47]. Within 15 minutes of adjusting the turbidity, a sterile cotton swab was immersed in the standardized suspension and gently streaked onto the dried agar surface to create a uniform lawn of inoculum. The plates were subsequently allowed to dry for 15 minutes with the lid in place to ensure proper adherence to the inoculum. Wells with a diameter of 6 mm were then aseptically punched into the solidified media using a sterile borer [48]. Using a micropipette, 100 μ L of the solution containing the test compound was carefully dispensed into each well. The plates were incubated at 37°C for 24 hours to evaluate antibacterial activity. To ensure reproducibility, the experiment was conducted in triplicate. After incubation, the inhibition zones around the wells were measured using a millimeter scale, indicating the antimicrobial efficacy against the tested microorganisms.

2.6. Evaluation of Anticancer Activity

The cytotoxic potential of the quinazoline ligand (WMS) and its manganese (II) complex was evaluated against breast cancer cells using the Sulforhodamine B (SRB) assay [50]. MCF7 cells, a widely used breast cancer cell line, were exposed to varying concentrations of the compounds ranging from 31.25 to 1000 μ g/mL for 24 hours to allow cellular attachment. Following the initial incubation, the treated cells were cultured for 48 hours at 37°C in a humidified 5% CO₂ atmosphere. Subsequently, the cells underwent fixing and staining with the Sulforhodamine B (SRB) protein-binding dye. After removing the excess stain and solubilizing the bound stain, the optical density was quantified at 564 nm using a microplate reader with automatic background correction. Mean values were computed for each concentration, and dose-response curves correlated compound concentration with cell viability. Untreated MCF7 cells were the negative control, while cisplatin-treated cells provided the positive control. The cytotoxic effect was assessed by relating surviving cell fraction to drug concentration, generating survival curves [51, 52]. Cell survival percentage was determined using the formula:

$$\text{Cell survival (\%)} = (\text{Mean OD of treated cells} / \text{Mean OD of untreated cells}) \times 100$$

The IC₅₀ values, the concentrations required to inhibit 50% cell growth, were determined for the quinazoline ligand and manganese complex. Cytotoxicity experiments were performed in triplicate against MCF7 cells to ensure reproducibility.

2.7. Molecular Docking Study

Molecular docking analysis was performed using the MOE 2015 software package to investigate the interaction between the quinazoline manganese (II) complex and a cancer-relevant target macromolecule. The three-dimensional structure of the target protein was obtained from the Protein Data Bank (PDB) website (PDB:3HB5) [35, 36]. The optimal structure of these compounds was generated using Material Studio software with the (DNP) basis sets, followed by docking of the complex to the target receptor. Additionally, MOE software analyzed the interaction between the protein and the quinazoline ligand (WMS) and its manganese complex.

2.8. Establishing of QCM-Based Nano Quinazoline Manganese Complex Sensor

The study utilized a QCM sensor consisting of an AT-cut quartz crystal chip with a 12 mm gold electrode resonating at 5 MHz (Q-Sense, Shenzhen, China) [52]. Before immobilizing the nanomaterial, the gold sensor underwent a thorough cleaning process. It was immersed in a solution containing aqueous ammonia, H₂O₂, and double-distilled water in a 5:1:1 volumetric ratio. The cleaning solution was maintained at 75°C, and the gold sensor was submerged for 10 minutes. After cleaning, the sensor was rinsed with double-distilled water and ethanol and then air-dried at ambient temperature. The dehydrated quartz crystal was carefully placed into the Q-Sense device. A stream of double-distilled water initially flowed over the electrode to establish a background electrolyte. This step allowed for baseline readings before introducing the nano-sized quinazoline manganese complex. The double-distilled water was continuously poured into the QCM module until the QCM signal stabilized; at this point, the signal value was set to zero. Following the baseline measurement, a solution was prepared by combining 2 mL of 1 ppm nano-sized quinazoline manganese complex with 10 mL of double-distilled water. This mixture was then injected into the gold sensor at a flow rate of 0.4 mL/min [52-55].

2.8.1. QCM Monitoring of Arsenic Ions

Quartz crystal microbalance (QCM) experiments were conducted using a commercial QCM system to monitor the binding of arsenic ions to the nano-sized quinazoline manganese complex sensors (Fig 1). The measurements involved injecting 1 ppm arsenic solutions over the sensor-coated QCM chips at controlled temperatures (20°C, 25°C, and 30°C) [56, 57] and pH values (3.5, 7, and 11) [58]. The arsenic solution was repeatedly injected until the sensor response stabilized, indicating that binding equilibrium was reached. After a set time, double-distilled water was flushed through the QCM module to remove any unbound arsenic and regenerate the sensor surface for subsequent measurements. This process provided insights into the interaction between the nano-complex sensors and arsenic ions under different environmental conditions.

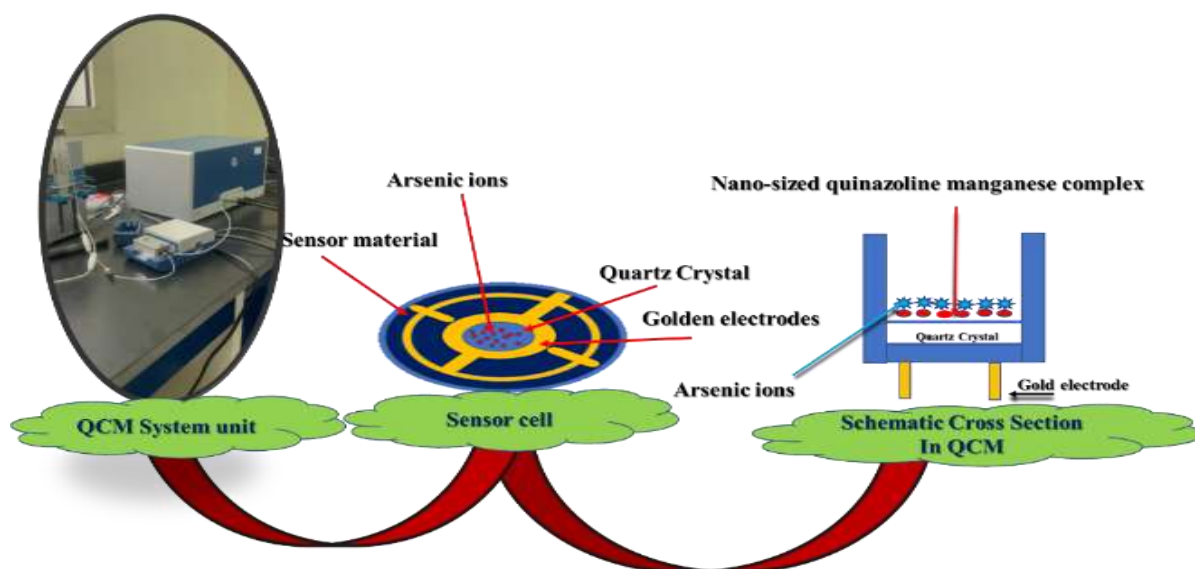


Fig 1. QCM Monitoring Setup for Arsenic Ion Binding to Nano-Sized Quinazoline Manganese Complex Sensors

3. Results and Discussion

3.1.1 Characterization of Quinazoline Manganese/Glycine Complex

The quinazoline manganese/glycine complex has a distinct chemical composition and notable biological properties. It is air-stable and soluble in polar organic solvents like dimethylformamide (DMF) and dimethyl sulfoxide (DMSO), but insoluble in water and ethanol. Elemental analysis confirms the 1:1:1 metal (**Mn (II)**) to ligand (**WMS**) to ligand (**Gly**) (**Mn: WMS: Gly**) ratio. The elemental analysis results for the quinazoline manganese/glycine complex ($C_{20}H_{26}ClMnN_7O_4$) are as follows: The calculated values were 46.25% for carbon (C), 5.01% for hydrogen (H), 18.90% for nitrogen (N), 6.83% for chlorine (Cl), and 10.58% for manganese (Mn). The experimentally found values were 46.08% for carbon, 4.88% for hydrogen, 18.77% for nitrogen, 6.72% for chlorine, and 10.46% for manganese. Conductivity assessments in dimethyl sulfoxide (DMSO) at a concentration of 10^{-3} M and a temperature of 25 °C indicated a molar conductivity value of $17 \Omega^{-1} \text{ mol}^{-1} \text{ cm}^2$, indicating the electrolytic nature of quinazoline manganese/glycine complex. The coordination of the hybrid ligands to the manganese center can be elucidated by comparing the infrared spectra of the parent quinazoline ligand and quinazoline manganese/glycine complex (Fig 2) (Table 1). The IR spectrum of (**WMS**) shows significant peaks at 1605 and 1545 cm^{-1} , attributed to the azomethine (C=N) and pyridine (C=N) groups, respectively (Fig 2A) [59-61]. In the metal complex (Fig 2B), these peaks shifted to higher wavenumbers of 1610 and 1560 cm^{-1} [62, 63]. A broad band at 3437 cm^{-1} is associated with the $\nu(\text{N-H})$ stretching vibration of coordinated water molecules [64, 65]. This shift strongly implies coordination involving the (C=N) groups. Two bands at 1421 and 1336 cm^{-1} correspond to the asymmetric and symmetric (COO^-) vibrations, indicating glycine's carboxylate group's involvement in metal coordination [66-68]. Furthermore, non-ligand bands at 460 and 506 cm^{-1} are assigned to $\nu(\text{M-N})$ and $\nu(\text{M-O})$, respectively [69, 70]. These observations suggest the quinazoline ligand (**WMS**) acts as a neutral tridentate coordinating through two azomethine nitrogens and the pyridine nitrogen, while glycine coordinates as a uninegative bidentate ligand via NH_2 and COO^- groups. Based on this data, the proposed formula for the manganese complex is $[\text{Mn}(\text{WMS})(\text{Gly})\text{H}_2\text{O}] \cdot \text{Cl} \cdot \text{H}_2\text{O}$. In the DFT calculation, the unique bands of the Quinazoline Manganese/Glycine Complex were compared with the experimental data, revealing significant peaks at 1629, 1575, 1466, 1360, 537, and 475 cm^{-1} . These peaks correspond to the azomethine (C=N), pyridine (C=N), asymmetric (COO^-), symmetric (COO^-), $\nu(\text{M-N})$, and $\nu(\text{M-O})$ vibrations, respectively. The experimental and theoretical IR data are in alignment, as shown in Fig 3. In the UV-Vis spectrum, the manganese complex exhibited $\pi-\pi^*$ conjugated system peaks at 279 and 316 nm, an $n-\pi^*$ transition at 347 nm, and a charge transfer band at 387 nm [71-73]. ESI-MS confirmed the manganese complex at $m/z = 465 [\text{M}+1]^+$, matching the calculated m/z of 464.39. The (**WMS**) and (**Gly**) ligand moieties were observed at 318.78 and 74.20 m/z , respectively, indicating complexation (Table 2). The molecular ions confirm the 1:1:1 **Mn (II): (WMS): (Gly)** stoichiometry. Thermal analysis of $[\text{Mn}(\text{WMS})(\text{Gly})\text{H}_2\text{O}] \cdot \text{Cl} \cdot \text{H}_2\text{O}$ showed four decomposition steps. The first step from 35-105°C (peak at 85°C) corresponded to the loss of hydrated water molecules, with a 3.05% mass loss (calc. 3.46%). The second step from 105-295°C (peak at 245°C) involved loss of $\text{C}_7\text{H}_{10}\text{NOCl}$, with a 29.99% mass loss (calc. 30.76%). The third step from 295-445°C (peak at 310°C) indicated the loss of $\text{C}_2\text{H}_4\text{NO}$, with a 10.49% mass loss (calc. 11.19%). The final step from 445-800°C (peak at 560°C) was related to the loss of $\text{C}_{11}\text{H}_{10}\text{N}_5$, with a 40.53% mass loss (calc. 40.90%). Manganese oxide (**MnO**) remained as the residue after complete decomposition. The antimicrobial activity of the Schiff base ligand (**WMS**) and its manganese (II) complex, $[\text{Mn}(\text{WMS})(\text{Gly})\text{H}_2\text{O}] \cdot \text{Cl} \cdot \text{H}_2\text{O}$. In addition, we investigated the antibacterial and antifungal properties of the manganese(II) Schiff base complex $[\text{Mn}(\text{WMS})(\text{Gly})\text{H}_2\text{O}] \cdot \text{Cl} \cdot \text{H}_2\text{O}$ and the free Schiff base ligand (**WMS**) using the disc diffusion method [74]. The study conducted experiments on different bacterial organisms, including Gram-positive bacteria such as *Streptococcus mutans* and *Staphylococcus aureus*, Gram-negative bacteria such as *Escherichia coli* and *Klebsiella pneumonia*, as well as fungal strains like *Candida albicans* and *Aspergillus niger* (Table 3). The results unequivocally highlighted the remarkable effectiveness of the manganese (II) complex against *Staphylococcus aureus*, exhibiting an inhibition zone of 14.3 ± 0.5 mm,

while the free Schiff base ligand showed no activity against this bacterium. Against *Klebsiella pneumoniae*, the manganese (II) complex demonstrated an inhibition zone of 27 ± 0.5 mm, comparable to the standard drug gentamicin (25 ± 0.5 mm), whereas the free ligand was inactive. For *Escherichia coli*, the manganese (II) complex displayed moderate activity with an inhibition zone of 13.9 ± 1.0 mm, lower than gentamicin (19.8 ± 0.5 mm), while the free ligand showed no activity. Against *Streptococcus mutans*, both the manganese (II) complex (10.9 ± 0.5 mm) and the free Schiff base ligand (17.4 ± 1.0 mm) exhibited inhibition zones, with the free ligand exhibiting higher activity than the complex and the standard drug ampicillin (28 ± 0.5 mm). Furthermore, the free Schiff base ligand exhibited high antifungal action against *Candida albicans* (12.3 ± 0.5 mm), outperforming the manganese (II) complex (15.3 ± 0.5 mm) and the standard drug nystatin (21 ± 0.5 mm). Against *Aspergillus niger*, both the manganese (II) complex (14.6 ± 0.5 mm) and the free Schiff base ligand (16 ± 0.5 mm) demonstrated moderate antifungal activity, lower than the standard drug nystatin (29 ± 0.5 mm) (Table 3). The anticancer activity of the Schiff base ligand (WMS) and its manganese (II) complex, $[\text{Mn}(\text{WMS})(\text{Gly})\text{H}_2\text{O}] \cdot \text{Cl} \cdot \text{H}_2\text{O}$, against the breast cancer cell line MCF7 [75]. The activity is expressed as the surviving fraction of cancer cells at different concentrations (12.5, 25, 50, and 100 $\mu\text{g}/\text{mL}$), and the IC_{50} value, which represents the concentration required to inhibit 50% of cell growth, is also provided. The data (Table 4) shows that the manganese (II) complex exhibits significantly higher anticancer activity than the free Schiff base ligand. The manganese (II) complex demonstrates a lower surviving fraction of MCF7 cells at all tested concentrations, indicating greater cytotoxicity and growth inhibition. Specifically, at the highest concentration of 100 $\mu\text{g}/\text{mL}$, the surviving fraction of MCF7 cells treated with the manganese (II) complex is only 16%, while the surviving fraction for the free ligand is 39.5%. This trend is consistent across all concentrations, with the complex consistently showing lower surviving fractions than the free ligand. The enhanced anticancer activity of the manganese (II) complex is further supported by its lower IC_{50} value of 12 $\mu\text{g}/\text{mL}$, compared to the free ligand's IC_{50} of 44.5 $\mu\text{g}/\text{mL}$. This indicates that the complex requires a significantly lower concentration to achieve 50% cell growth inhibition, making it a more potent anticancer agent against the MCF7 breast cancer cell line. The improved anticancer activity of the manganese (II) complex can be attributed to several factors related to the complexation of the Schiff base ligand with the manganese (II) ion. Complexation can enhance the lipophilicity and cellular uptake of the compound, facilitating its entry into cancer cells and increasing bioavailability [76,77]. Additionally, the presence of the metal ion can induce the generation of reactive oxygen species (ROS), which can damage cellular components and trigger apoptosis (programmed cell death) in cancer cells.

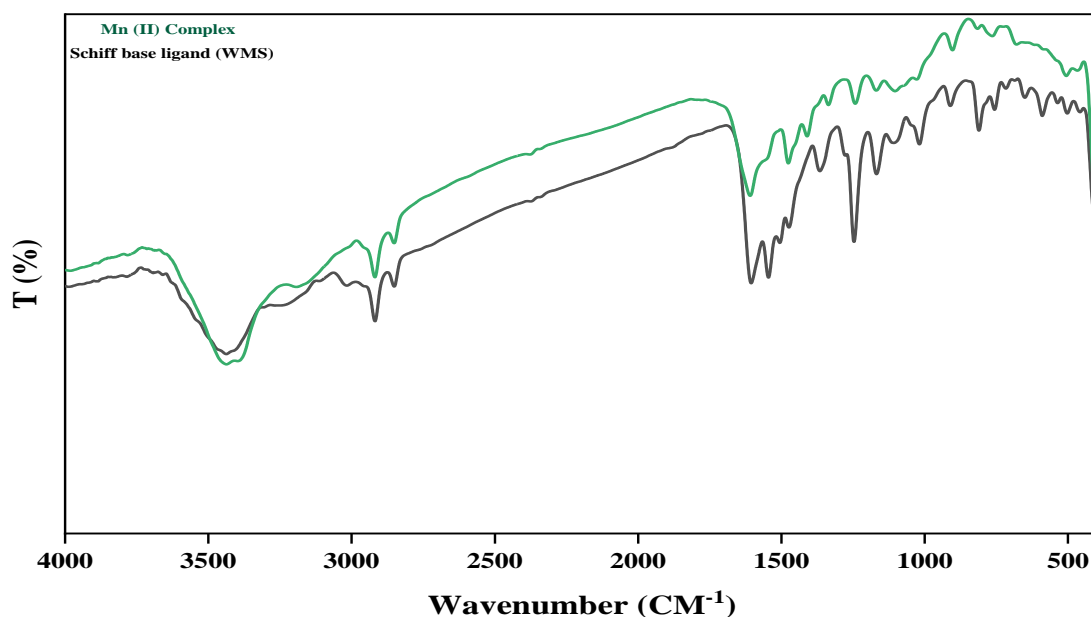
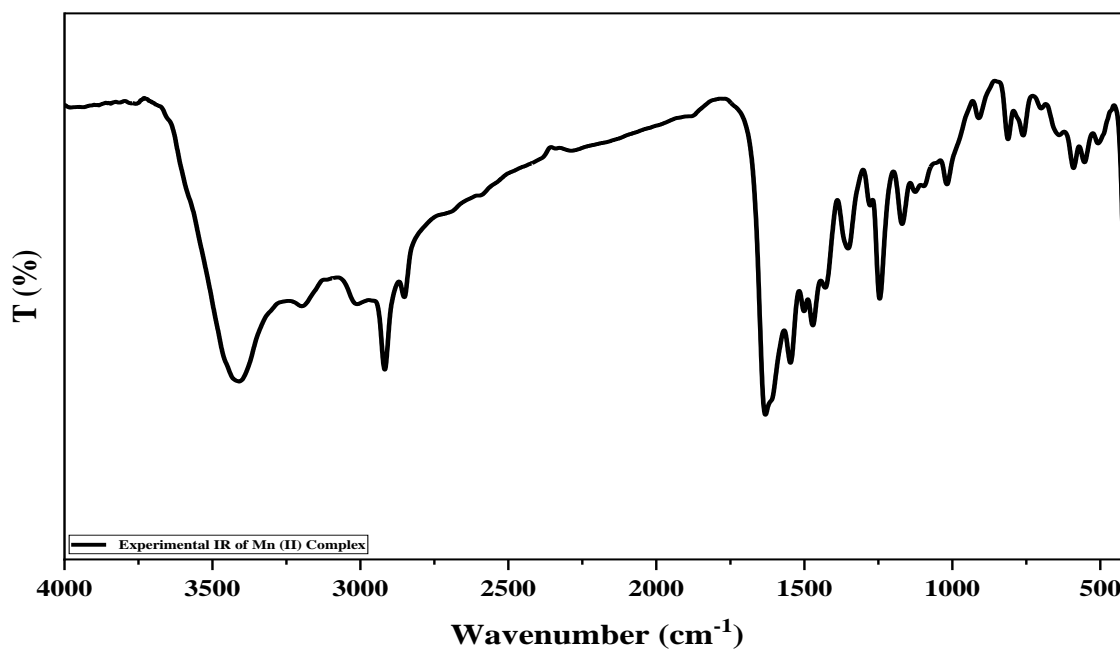
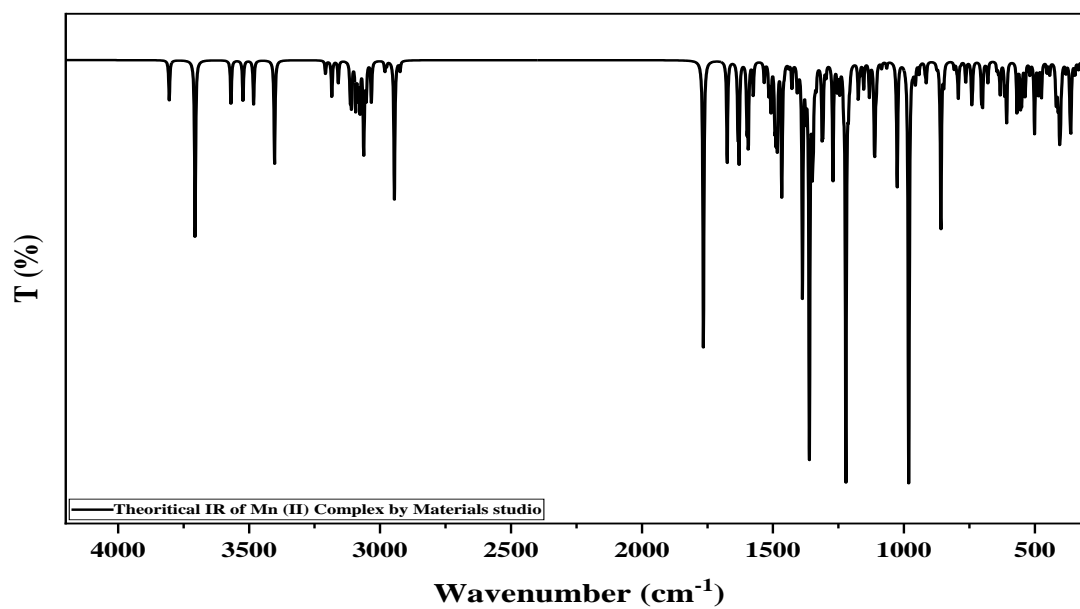


Fig 2. Comparative Infrared Spectra of the Parent Quinazoline Ligand and the Quinazoline Manganese/Glycine Complex.



(A)



(B)

Fig 3. Comparison of Experimental (A) and Theoretical (B) IR Spectra of the Quinazoline Manganese/Glycine Complex

Table 1. The most significant infrared (IR) spectral bands of the isolated Schiff base ligand ternary Manganese Complex are as follows.

Compound	$\nu(\text{C}=\text{N})$	$\nu(\text{C}=\text{N})$ Pyridine ring	$\nu(\text{COO})_{\text{Asymmetric}}$ glycine	$\nu(\text{COO})_{\text{Symmetric}}$ glycine	$\nu(\text{M}-\text{O})$	$\nu(\text{M}-\text{N})$
	Schiff base ligand (WMS)	1605 sh	1545 sh	-----	-----	-----
$[\text{Mn}(\text{WMS})(\text{Gly})\text{H}_2\text{O}] \cdot \text{Cl} \cdot \text{H}_2\text{O}$	1610 m	1560 sh	1421 sh	1336 sh	506 m	460 w

Table 2. ESI-MS Data for the Quinazoline Manganese/Glycine Complex and Its Ligand (WMS) Moieties.

Compound	m/z value		Interpretation
	Calculated	Found	
Schiff base ligand (WMS)	318.38	318.78	$[\text{M}]^+$
Glycine (Gly)	75.07	74.20	$[\text{M}]^+$
$[\text{Mn}(\text{WMS})(\text{Gly})\text{H}_2\text{O}] \cdot \text{Cl} \cdot \text{H}_2\text{O}$	464.39	465	$[\text{M}+1]^+$

Table 3. Antibacterial and Antifungal Activity of the Manganese (II) Schiff Base Complex $[\text{Mn}(\text{WMS})(\text{Gly})\text{H}_2\text{O}] \cdot \text{Cl} \cdot \text{H}_2\text{O}$ and Free Schiff Base Ligand (WMS).

Sample	(1)		Standard drug
	SCHIFF BASE LIGAND (WMS)	$[\text{Mn}(\text{WMS})(\text{Gly})\text{H}_2\text{O}] \cdot \text{Cl} \cdot \text{H}_2\text{O}$	
Gram-negative bacterial			Gentamicin
<i>Escherichia coli</i> (ATCC: 10536)	13.9±1.0	19.8±0.5	27 ±0.5
<i>Klebsiella Pneumonia</i> (ATCC: 10031)	NA	24.0±1.0	25 ±0.5
Gram-positive bacteria			Ampicillin
<i>Staphylococcus Aureus</i> (ATCC: 13565)	NA	14.3±0.5	20 ±0.1
<i>Streptococcus mutans</i> (ATCC: 25175)	10.9±0.5	17.4±1.0	28 ±0.5
Fungi			Nystatin
<i>Candida Albicans</i> (ATCC: 10231)	15.3±0.5	12.3±0.5	21 ±0.5
<i>Aspergillus Nigar</i> (ATCC: 16404)	14.6±0.5	16±0.5	29±0.5

TABLE 4. Anticancer Activity of the Schiff Base Ligand (**WMS**) and Its Manganese (II) Complex $[\text{Mn}(\text{WMS})(\text{Gly})\text{H}_2\text{O}]\cdot\text{Cl}\cdot\text{H}_2\text{O}$ Against MCF7 Breast Cancer Cell Line.

Compounds	Conc. ($\mu\text{g/mL}$)				IC_{50} ($\mu\text{g/mL}$)
	12.5	25	50	100	
	Surviving fraction (MCF7)				
Schiff base ligand (WMS)	92	72	44	39.5	44.5
$[\text{Mn}(\text{WMS})(\text{Gly})\text{H}_2\text{O}]\cdot\text{Cl}\cdot\text{H}_2\text{O}$	48	42	23.5	16	12

3.1.2. Computational Investigations

Density Functional Theory (DFT) was employed to optimize the geometry of the quinazoline ligand (**WMS**) and its manganese (II) complex. The fully optimized geometries and atomic numbering are depicted in Table 5. Analysis of the calculated bond lengths and angles (refer to Table 6) revealed a distorted octahedral geometry around the Mn (II) ion [78, 79]. Detailed data, including bond lengths and angles, are provided in Supplementary Table 1. The Mn (II) complex exhibited subtle elongations in certain bond lengths such as N(7)-N(8), N(8)-C(9), C(10)-N(11), N(11)-N(12), C(15)-N(14), and N(14)-C(13) [80] due to coordination of **WMS** via its two azomethine nitrogens and pyridine nitrogen. Global reactivity descriptors, including the HOMO-LUMO energy gap (ΔE), ionization potential (I), electron affinity (A), chemical potentials (μ), absolute electronegativity (χ), absolute hardness (η), global softness (S), global electrophilicity (ω), and additional electronic charge (ΔN_{max}) [81, 82] were computed for both **WMS** and its Mn(II) complex using consistent computational methods, with detailed results in Table 6. These properties were calculated using formulas: absolute hardness $\eta = (I - A)/2 = (E_{\text{LUMO}} - E_{\text{HOMO}})/2$, global softness $S = 1/2\eta$, chemical potential $\mu = -(I + A)/2$, electronegativity $\chi = (I + A)/2 = (E_{\text{LUMO}} + E_{\text{HOMO}})/2$, HOMO-LUMO gap $\Delta E = E_{\text{LUMO}} - E_{\text{HOMO}}$, absolute softness $\sigma = 1/\eta$, and $\Delta N_{\text{max}} = -1/\eta$. A reduced energy gap suggests charge transfer interactions influencing biological activity. The gap indicates chemical reactivity, with a narrower frontier orbital gap corresponding to higher reactivity ("soft" molecule). It also serves as a stability index for structural and conformational barriers. For (**WMS**), the gap was 2.053 eV, while for its Mn(II) complex, it was 0.723 eV, with a higher gap indicating greater stability. The chemical potential (μ) was negative, while the electrophilicity index (ω) was positive, suggesting **WMS** likely acts as an electron donor to the metal ions [83, 84].

Table 5. Optimized geometry visualization of the studied (**WMS**) and its Manganese (II) Complex $[\text{Mn}(\text{WMS})(\text{Gly})\text{H}_2\text{O}]\cdot\text{Cl}\cdot\text{H}_2\text{O}$.


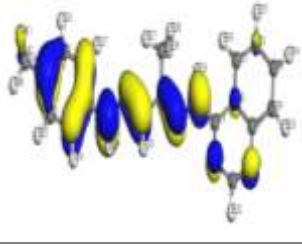
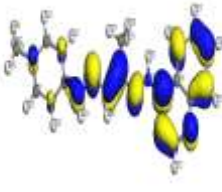
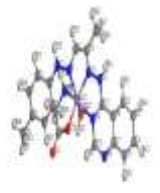


Optimized geometry visualization of the studied (WMS) and its Ternary Mn (II) Complex				
Compound	optimized structure	3D-HOMO	3D-LUMO	ΔE (eV)
(WMS)				$E_{\text{HOMO}} = -4.177$ eV $E_{\text{LUMO}} = -2.124$ eV 2.053
$[\text{Mn}(\text{WMS})(\text{Gly})\text{H}_2\text{O}]\cdot\text{Cl}\cdot\text{H}_2\text{O}$				$E_{\text{HOMO}} = -6.873$ eV $E_{\text{LUMO}} = -6.150$ eV 0.723

TABLE 6. Optimized and Quantum Chemical Parameters for (WMS) and its Manganese (II) Complex [Mn(WMS)(Gly)H₂O]·Cl·H₂O: A Comparative Analysis

The calculated quantum chemical parameters	(WMS)	[Mn(WMS)(Gly)H ₂ O]·Cl·H ₂ O
E _{HOMO} (eV)	-4.177eV	-6.873 eV
E _{LUMO} (eV)	-2.124eV	-6.150 eV
ΔE (eV)	2.053	0.723
χ(eV)	3.1505	6.5115
η(eV)	1.0265	0.3615
σ(eV) ⁻¹	0.974184121	2.766251729
Πi (eV)	-3.1505	-6.5115
S (eV) ⁻¹	0.48709206	1.383125864
ω(eV)	4.834705431	58.64402801
ΔN _{max}	3.069167073	18.01244813
Bond lengths (Å)	(WMS)	[Mn(WMS)(Gly)H₂O]·Cl·H₂O
N(7)-N(8)	1.343	1.363
N(8)-C(9)	1.305	1.363
C(10)-N(11)	1.317	1.365
N(11)-N(12)	1.355	1.391
C(15)-N(14)	1.357	1.386
N(14)-C(13)	1.332	1.360
Bond angles (o)	(WMS)	[Mn(WMS)(Gly)H₂O]·Cl·H₂O
O(33)-Mn(25)-N(29)	-----	82.664
O(33)-Mn(25)-O(26)	-----	88.357
O(33)-Mn(25)-N(14)	-----	93.88
O(33)-Mn(25)-N(11)	-----	170.808
O(33)-Mn(25)-N(8)	-----	108.338
N(29)-Mn(25)-O(26)	-----	55.702
N(29)-Mn(25)-N(14)	-----	131.998
N(29)-Mn(25)-N(11)	-----	105.502
N(29)-Mn(25)-N(8)	-----	87.701
O(26)-Mn(25)-N(14)	-----	76.403
O(26)-Mn(25)-N(11)	-----	92.806
O(26)-Mn(25)-N(8)	-----	138.034
N(14)-Mn(25)-N(11)	-----	77.56
N(14)-Mn(25)-N(8)	-----	137.33
N(11)-Mn(25)-N(8)	-----	76.669

3.1.3. Docking study

The Schiff base ligand and its Mn (II) complex were subjected to computational molecular docking analysis using the Molecular Operating Environment (MOE, version 2015.10) software [85, 86]. This analysis was performed to (PDB ID: 3HB5) as the receptor [35, 36]. All structural optimizations were conducted within MOE until reaching a root mean square deviation (RMSD) gradient of 0.05 kcal mol⁻¹ Å⁻¹ using the MMFF94x force field, and the partial charges were automatically assigned. The PDB entry 3HB5 provides valuable structural insights into the interactions of the human estrogen receptor alpha (ERα) with ligands, an important target for breast cancer therapy. It represents the crystal structure of the ligand-binding domain of ERα in complex with the agonist diethylstilbestrol (DES). ERα is a nuclear hormone receptor that regulates gene expression involved in cell growth, differentiation, and reproductive functions; its activity is closely linked to the development and progression of hormone-dependent breast cancers. Inhibiting or modulating this receptor can significantly impact the proliferation of cancer cells. The publication by Gangloff et al. (2001) describes the detailed structural analysis of the ERα-DES complex, providing insights into how the agonist binds within the receptor's ligand-binding pocket. This complex structure reveals the conformational changes and the stabilization of the receptor in its active form, which is crucial for understanding the molecular mechanisms underlying receptor activation and hormone signaling. Furthermore, the 3HB5 structure highlights the key interactions between ERα and DES, which can guide the design and development of new selective estrogen receptor modulators (SERMs) and antagonists for improved breast cancer treatments. By elucidating the binding modes and structural

dynamics of ER α , this structure aids in the rational design of compounds that can either inhibit or modulate the receptor's activity, offering potential therapeutic strategies for managing estrogen receptor-positive breast cancers. Overall, the 3HB5 structure is an important contribution to understanding ER α as a drug target and developing improved therapeutics for breast cancer therapy. In the realm of experimental observations, the (WMS) demonstrated a noteworthy IC₅₀ value of 44.5 $\mu\text{g/ml}$ when assessed against a breast cancer cell line. Furthermore, the quinazoline manganese (II) complex is denoted as [Mn(WMS)(Gly)H₂O]·Cl·H₂O, derived from the aforementioned ligand, exhibited enhanced anticancer efficacy, displaying reduced IC₅₀ values of 12 $\mu\text{g/ml}$. To validate these findings, theoretical docking studies focused on the (PDB ID: 3HB5), a vital target for Breast cancer therapy. Docking analysis outcomes using (PDB ID: 3HB5) indicated that both the (WMS) and its [Mn(WMS)(Gly)H₂O]·Cl·H₂O displayed notably low binding energies of -1.3 and -9.1 kcal mol⁻¹, respectively. This implies heightened activity in the quinazoline manganese (II) complex compared to the original ligand (WMS), owing to the establishment of coordination bonds with the Manganese (II) metal ion. The results of docking simulations for ligand (WMS) and its Mn (II) complex are depicted through both two-dimensional (2D) and three-dimensional (3D) representations, as presented in Fig 4. Furthermore, Table 7 elucidates the binding energies associated with the Schiff base ligand (WMS) and its Mn (II) complex.

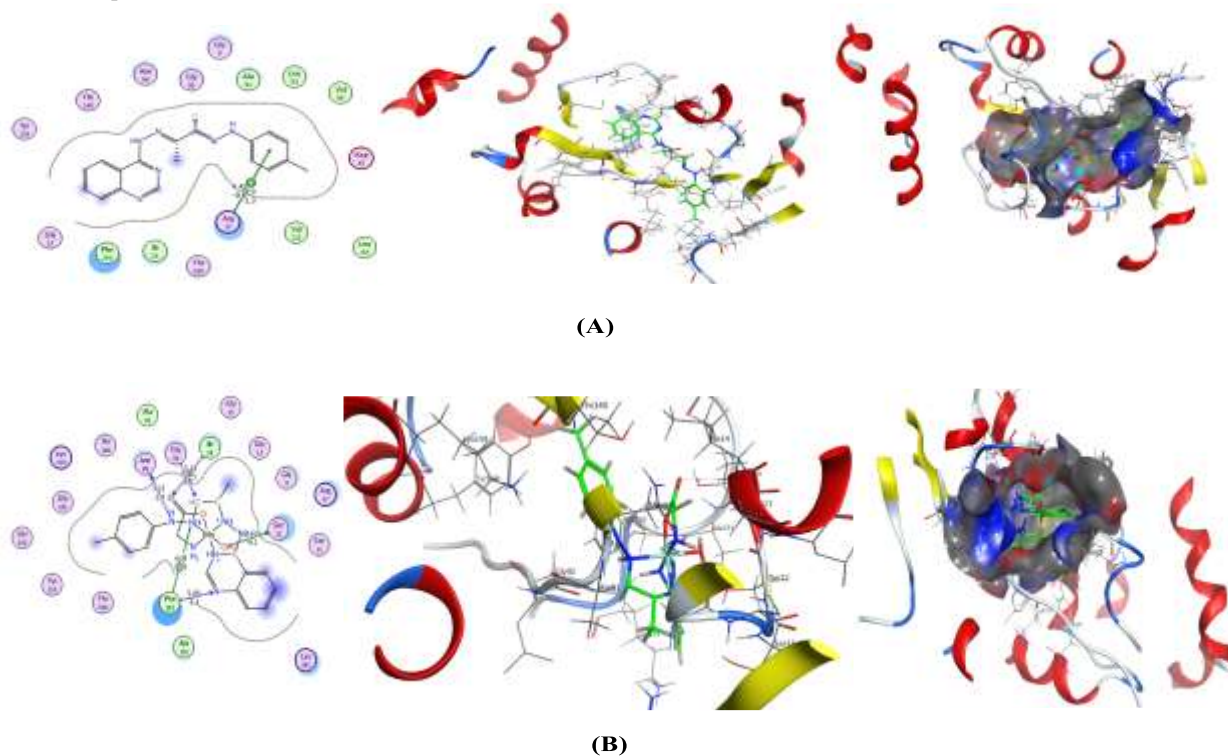


Fig 4. Visual Representation of Breast Cancer Receptor (PDB: 3HB5) Interaction with (A) (WMS) Ligand and (B) its Mn (II) Complex: Comparative 2D & 3D Diagrams (isolated and inside pocket view).

Table 7. Results of docking interactions to 3HB5 bound to tubulin in cancer cell with ligand (WMS) and its Mn (II) complex

Cancer cell Receptor	Cpds	Ligand moiety	Receptor site	Interaction	Distance (Ao)	E (kcal/mol)
3HB5	Ligand	6-ring	NE ARG 37 (X)	pi-cation	3.90	-1.3
		6-ring	NH2 ARG 37 (X)	pi-cation	4.41	-0.6
	Mn complex	N 7	O ASN 90 (X)	H-donor	3.21	-1.9
		O 29	OG SER 12 (X)	H-donor	2.63	-9.1
		C 10	N GLY 92 (X)	H-acceptor	3.06	-2.6
		N 19	N PHE 192 (X)	H-acceptor	3.44	-1.1
		O 35	N ILE 14 (X)	H-acceptor	3.21	-1.3
		N 8	6-ring PHE 192 (X)	H-pi	4.74	-0.9

3.2. Characterization of Nano-Quinazoline Manganese/Glycine Complex

3.2.1. XRD

Recent advances in powder X-ray diffraction (XRD) have enhanced the ability to investigate the physicochemical makeup of unknown materials. XRD remains a prevalent technique for determining unit cell dimensions and symmetry, providing qualitative, quantitative, and other analytical information [87, 88]. The translation symmetry and unit cell features can be deduced from the peak positions in the diffraction pattern. The size and shape of the unit cell can be elucidated by identifying several Bragg reflections. In this case, reflections at 2θ values of 19.695° , 21.176° , 28.558° , 31.032° , 31.884° , 32.839° , 33.728° , 35.833° and 36.158° correspond to the (100), (101), (111), (200), (112), (201), (002), (210), and (103) planes, respectively. By examining the allowed reflections for different cubic crystal structures, it becomes evident that these planes fit the criteria for a simple cubic (sc) lattice. The observed combination of Miller indices, including planes with mixed indices like (101), (112), (201), and (210), is characteristic of a cubic crystal structure. Therefore, based on the provided XRD data and the identified Miller indices (Fig 5), it can be concluded that the Schiff base quinazoline manganese/glycine complex exhibits a face-centered cubic (FCC) crystal structure.

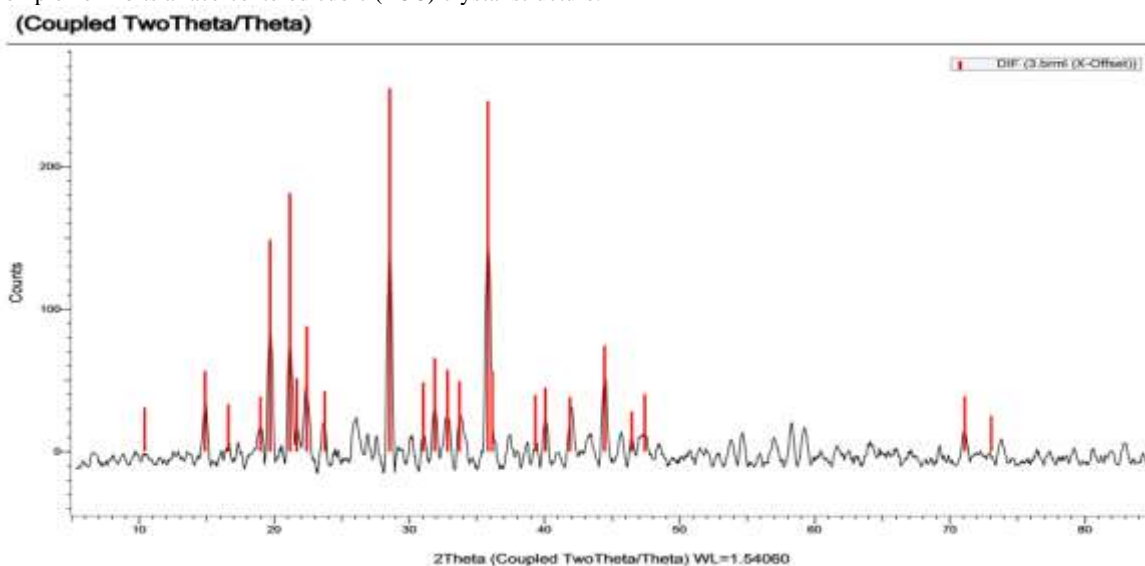


Fig 5. XRD Pattern of the Nano-Quinazoline Manganese/Glycine Complex Showing Bragg Reflections and Identified Miller Indices.

3.2.2. Textural Characters (AFM) of Schiff Base Quinazoline Manganese/Glycine Complex

The atomic force microscopy (AFM) images provide valuable insights into the surface morphology and textural characteristics of the Nano Schiff base quinazoline manganese/glycine complex [89]. The 3D perspective AFM image reveals a rough and uneven surface topography exhibiting a distinct pattern resembling waves or ripples, suggesting the presence of periodic structures or features. The height variations, represented by the color contrast, range from approximately 0 nm to 90 nm [90]. The 2D AFM image displays a characteristic granular or grainy texture, with irregularly shaped domains or grains randomly distributed across the surface. These domains vary in size and shape, indicating surface heights or material composition variations. The observed surface roughness, periodic structures, granular texture, and heterogeneous domain distribution suggest that the Schiff base quinazoline manganese/glycine complex possesses a complex surface morphology influenced by the formation of distinct surface features, crystalline domains, or specific morphological characteristics during the synthesis or crystallization process. Analysis revealed the particles had a size of 89 nm (Fig 6).

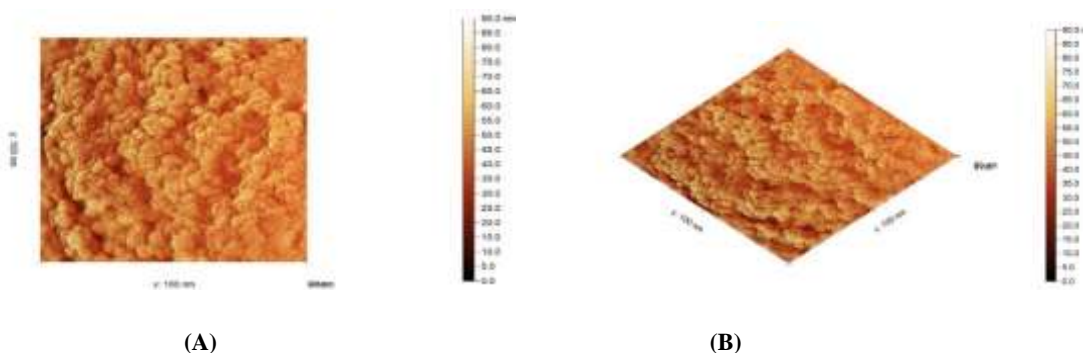
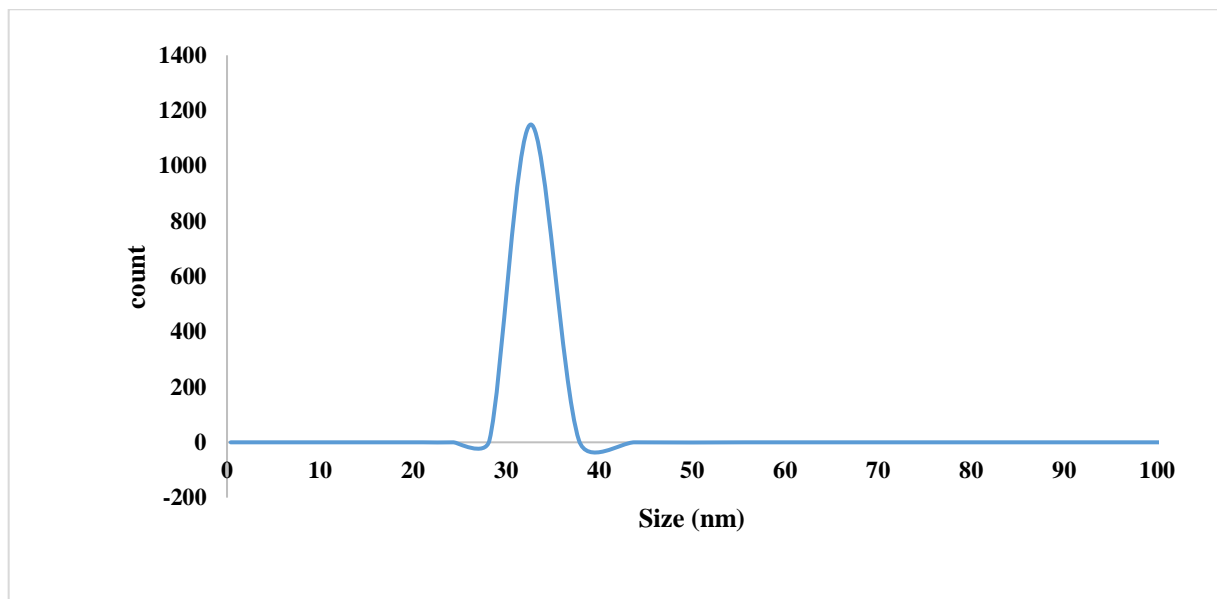


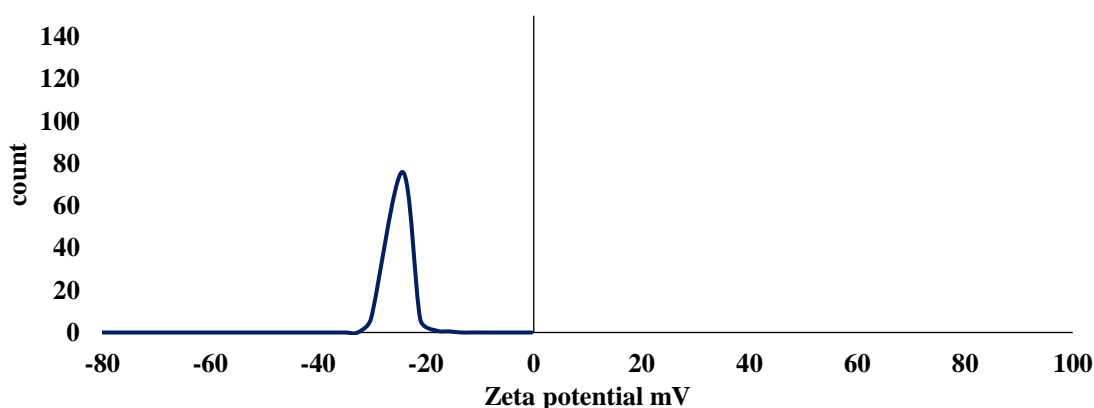
Fig 6. (A) Two-dimensional AFM Visualization and (B) Three-dimensional AFM Image of the Nano Schiff base quinazoline manganese/glycine complex.

3.2.3. DLS and Zeta Potential

The nanoparticle size distribution and colloidal stability of the synthesized nano-sized quinazoline manganese complex were evaluated using dynamic light scattering (DLS) analysis [91, 92]. The results revealed that the nano-sized quinazoline manganese complex had an average particle size of 32.67 nm (Fig 7A), exhibiting a uniform size distribution with a low polydispersity index. This low polydispersity indicates that the nano-quinazoline manganese suspension possesses remarkable colloidal stability and uniformity in particle size distribution [93]. Furthermore, the zeta potential measurement of the nano-sized quinazoline manganese complex was found to be -24.363 mV (Fig 7B). The zeta potential value is a crucial parameter reflecting the physicochemical stability of nanoparticles during storage and handling [92]. A higher absolute zeta potential value generally corresponds to greater overall system stability, as it indicates stronger repulsive forces between nanoparticles, preventing agglomeration [94]. The obtained narrow particle size distribution and moderately negative zeta potential suggest that the synthesized nano-quinazoline manganese complex possesses exceptional colloidal stability and uniform dispersion characteristics [95,96]. These properties are highly desirable for various nanoparticle applications, ensuring consistent performance and prolonged stability during storage and utilization.



(A)



(B)

Fig 7. (A) Particle Size Distribution and (B) Zeta Potential Analysis of the Nano Schiff base quinazoline manganese/glycine complex

3.2.4. BET surface area and pore size.

The BET (Brunauer-Emmett-Teller) method is widely used to determine nanomaterials' surface area and pore size distribution [97]. According to the data provided by analysis (Fig 8), the following information can be extracted: The multipoint BET surface area for the nano-sized quinazoline manganese complex sample is **46.1536 m²/g**. The BET surface area provides a measure of the total accessible surface area of the material, which is a crucial parameter for applications involving adsorption, catalysis, and other surface-related processes [98-100]. The sample's average pore size (or average pore radius) is **7.4843 nm**, as determined from the pore size distribution analysis. This value indicates that the material possesses mesopores, which are pores with diameters between 2 and 50 nm. Additionally, the report provides information on the pore volume and pore size distribution obtained from different methods, such as the BJH (Barrett-Joyner-Halenda) method and the DFT (Density Functional Theory) method. For instance, the BJH adsorption cumulative pore volume is 0.150075 cc/g, and the DFT method cumulative pore volume is 0.1581 cc/g. The presence of a significant BET surface area and mesoporous structure can be advantageous for applications involving adsorption or catalysis, as it provides a high surface area for interaction with the target species and facilitates accessibility to the active sites within the material.

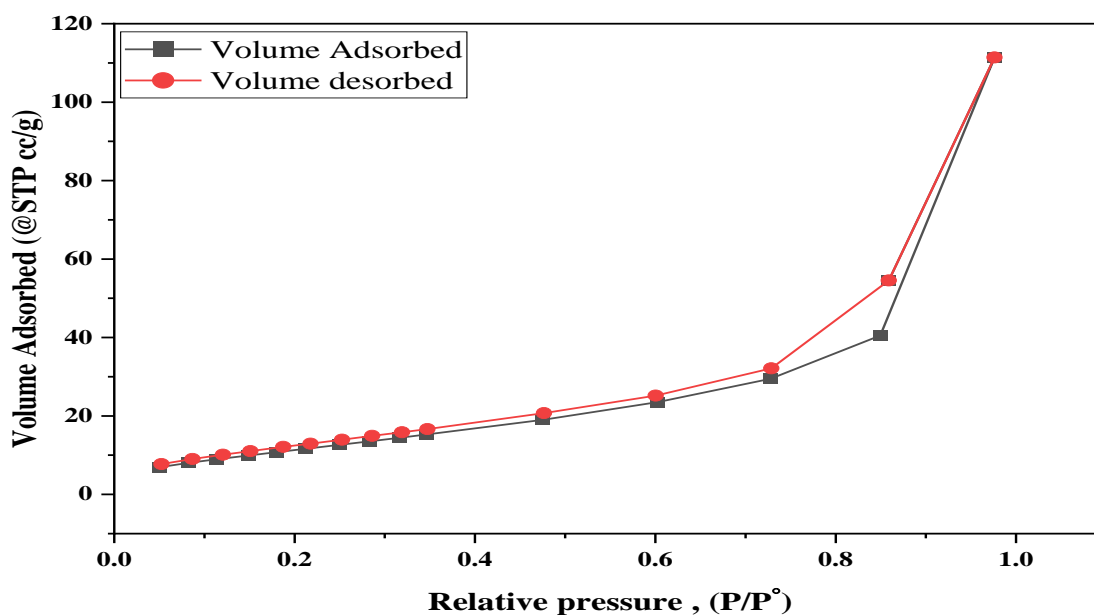


Fig 8. Illustrates the N₂-isotherm of the Nano Schiff base quinazoline manganese/glycine complex

3.2.5. Contact angle, hydrophobicity, and toxicity of the nano-sized quinazoline manganese complex.

The wettability and hydrophobicity of nanomaterials play a crucial role in their potential applications, particularly in aqueous environments [101-103]. The nano-sized quinazoline manganese complex exhibited remarkable hydrophobic characteristics, as evidenced by an impressive water contact angle of 123.7° (Fig 9). This inherent hydrophobicity opens up exciting prospects for utilizing these nanoparticles as highly sensitive and selective sensors in aqueous environments. Encouragingly, a comprehensive cytotoxicity evaluation unveiled an IC₅₀ value (the concentration at which 50% of cells are viable) of 479.31 µg/mL for the nano-sized quinazoline manganese complex. This notably high IC₅₀ value suggests a low cytotoxic potential, making it a promising candidate for water-related sensing applications without posing significant health risks [104-105]. It is crucial to note that the hydrophobicity of nanomaterials can be attributed to their surface chemistry, morphology, and composition. In the case of the nano-sized quinazoline manganese complex, the presence of organic ligands or functional groups could contribute to the observed hydrophobic nature. Additionally, the nanoparticle's size and shape can influence wettability, with smaller particles often exhibiting higher hydrophobicity due to their increased surface curvature. Furthermore, the low cytotoxicity of the nano-sized quinazoline manganese complex can be attributed to its unique chemical composition and structural properties. Manganese-based complexes have shown promising biocompatibility profiles, and the presence of quinazoline moieties could further enhance the material's biological tolerance. It is important to note that while the reported IC₅₀ value is encouraging, a comprehensive toxicological evaluation encompassing various cell lines, animal models, and diverse exposure routes is necessary to assess these nanoparticles' safety and environmental impact fully. Rigorous testing and adherence to regulatory guidelines are crucial steps before implementing the nano-sized quinazoline manganese complex in real-world applications.

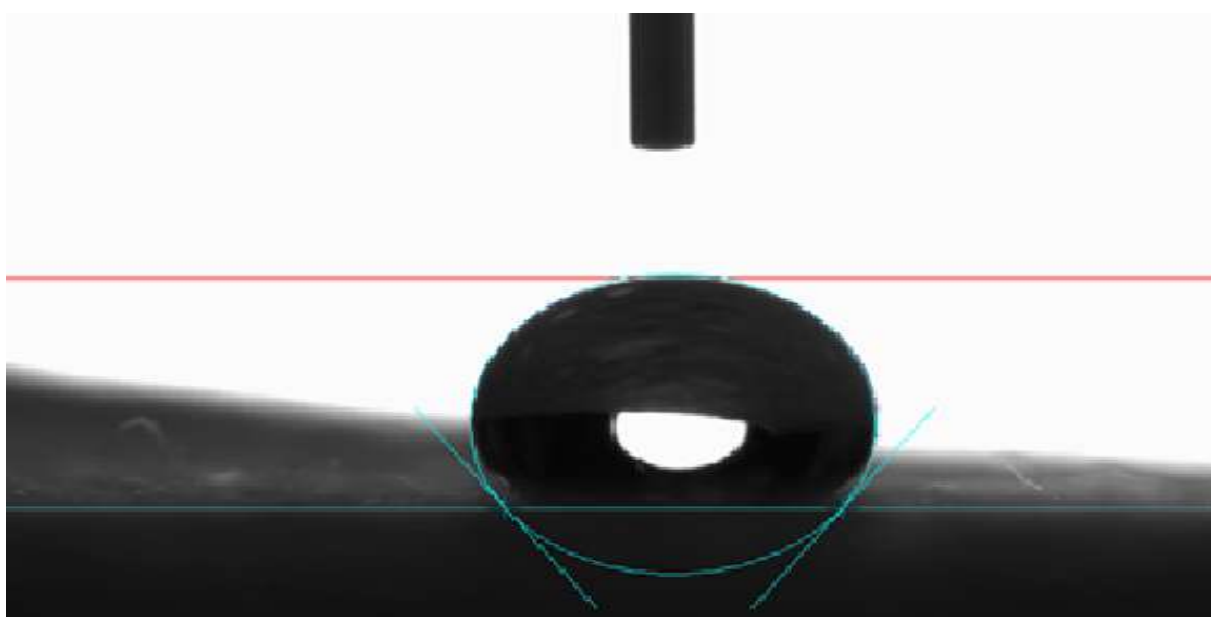


Fig 9. Water Contact Angle Measurement of the Nano-Quinazoline Manganese Complex Indicating Hydrophobicity

3.2.6. Arsenic ion monitoring using QCM-based nano quinazoline manganese sensors.

A typical experiment employing a Quartz Crystal Microbalance (QCM) based-nano quinazoline manganese sensor for detecting arsenic ions can be divided into four distinct stages, each providing crucial insights into the sensor's performance [106-109]. In the initial stage, the sensor's frequency response is recorded to establish a stable baseline measurement, which serves as a reference point for subsequent stages. This baseline stability is essential for accurate quantification of the sensor's response to arsenic ions. A sudden and significant decrease in the sensor's frequency is observed upon the introduction of arsenic ions. This rapid change is attributed to the swift binding of arsenic ions to numerous vacant sites on the sensor's surface. The frequency drop is directly proportional to the mass of arsenic ions adsorbed onto the sensor's surface. As the experiment progresses, further adsorption of arsenic ion molecules occurs on the nano quinazoline manganese sensor's surface. This stage demonstrates the sensor's ability to capture additional arsenic ions, indicating its potential for quantitative analysis and monitoring of arsenic concentrations. Eventually, an equilibrium state is reached in the adsorption process between the nano quinazoline manganese complex and the arsenic ion molecules. The sensor's frequency shift stabilizes at this point, indicating that the maximum capacity for arsenic ion adsorption has been attained. Once the frequency stabilizes, it signifies the attainment of an equilibrium state in the adsorption of arsenic ions on the QCM-based quinazoline manganese nanosensor's surface. At this fourth stage, no noticeable changes in the sensor's frequency are observed, implying minimal mass loss and minor structural modifications to the nanosensor's surface. Consequently, this reaffirms the sensor's effectiveness in detecting arsenic ions.

3.2.7. sensing mechanism of the QCM-based nano quinazoline manganese complex for arsenic ions

The proposed sensing mechanism of the QCM-based nano quinazoline manganese complex for arsenic ions involves various intermolecular interactions [110-113]. Due to the lower electronegativity of arsenic ions compared to the nano quinazoline manganese sensor, dipole-dipole interactions may arise, complemented by π - π interactions between the aromatic quinazoline moieties and the arsenic ions. Additionally, the presence of polar functional groups, such as nitrogen-containing heterocycles in the nano quinazoline manganese complex, can contribute to an increased density of negative charge on the sensor's surface. Consequently, the QCM-based nano quinazoline manganese sensor exhibits a heightened propensity for interaction with arsenic ions, primarily through electrostatic interactions facilitated by the negatively charged surface, alongside the π - π interactions between the aromatic quinazoline moieties and the arsenic ions [114]. This synergistic effect of multiple intermolecular interactions contributes to the sensor's high sensitivity and selectivity towards arsenic ions. It is worth noting that the specific sensing mechanism and the extent of intermolecular interactions may vary depending on the exact chemical composition, structural features, and experimental conditions of the nano-quinazoline manganese complex. Further investigations, including computational modeling and spectroscopic studies, could provide deeper insights into the detailed mechanisms involved in detecting arsenic ions by these nanosensors.

3.2.7.1. Effect of Temperature

The nano-quinazoline manganese complex exhibits a significant frequency shift in response to the presence of arsenic ions in the solution (Fig 10). This frequency shift is crucial for monitoring and detecting arsenic ions using the quartz crystal microbalance (QCM) technique. The graph shows three curves representing the frequency shift (Δf) at different temperatures: 20°C (blue curve), 25°C (green curve), and 30°C (red curve). Initially, all three curves exhibit a rapid and substantial drop in frequency, indicating the swift binding of arsenic ions to the surface of the nano-quinazoline manganese complex sensor. The magnitude of the initial frequency drop varies among the different temperature curves. The curve at 30°C (red) displays the

most substantial initial frequency drop, suggesting that higher temperatures may facilitate adsorption and result in a more pronounced sensor response. After the initial rapid decrease, the curves tend to stabilize, indicating an equilibrium state between the adsorption and desorption processes has been reached. The frequency shift remains relatively constant, implying a saturation of the available binding sites on the sensor's surface. Interestingly, the equilibrium frequency shift values differ among the three temperature curves. The curve at 20°C (blue) exhibits the smallest equilibrium frequency shift, while the curve at 30°C (red) shows the largest equilibrium frequency shift. Lower temperatures generally result in reduced kinetic energy of the metal ion and adsorbent particles, leading to fewer collisions and a slower adsorption process [115]. The higher kinetic energy of the particles at this temperature facilitates more frequent collisions and improves the diffusion of lead ions onto the adsorbent's surface [116]. This observation suggests that higher temperatures may enhance the overall adsorption capacity and sensitivity of the nano-quinazoline manganese complex sensor towards arsenic ions.

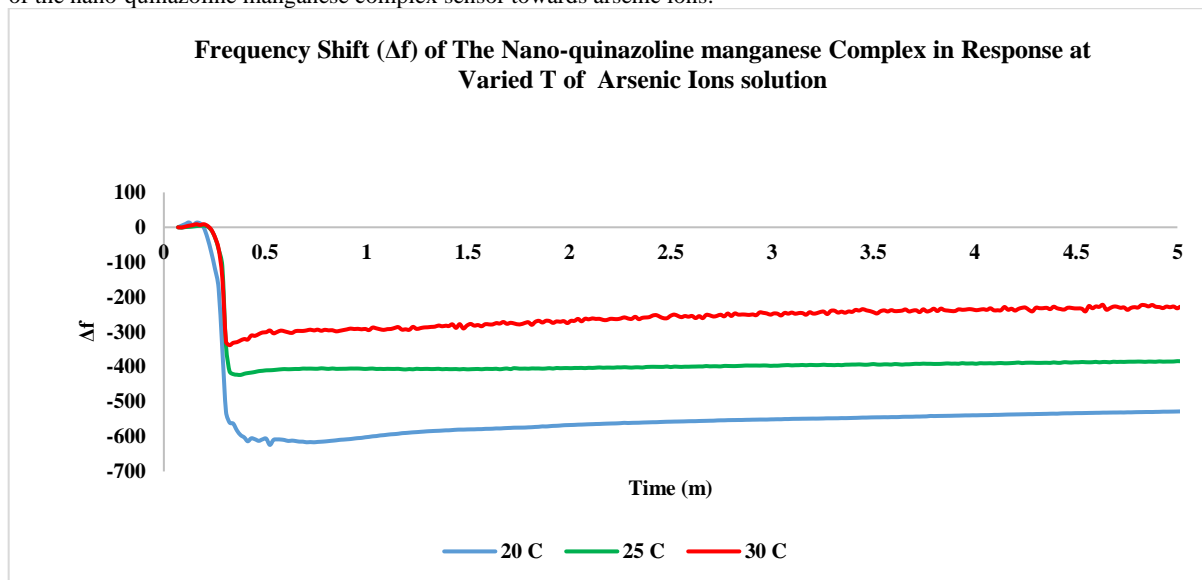


Fig 10. Frequency Shift (Δf) of the Nano-Quinazoline Manganese Complex Sensor in Response to Arsenic Ions at Different Temperatures (20°C, 25°C, 30°C).

3.2.7.2. Effect of pH

The pH of the solution plays a pivotal role in the adsorption of arsenic ions onto the nano-quinazoline manganese complex sensor, as evidenced by the varying frequency shifts observed at different pH values [117,118]. The graph depicts the frequency shift response of the sensor at three distinct pH levels: 3.5, 7, and 11 (Fig 11). At pH 3.5 (blue curve), the sensor exhibits a rapid and substantial initial frequency drop, indicating efficient adsorption of arsenic ions onto the sensor's surface. This behavior can be attributed to the protonation of functional groups on the nano-quinazoline manganese complex, facilitating electrostatic interactions with the positively charged arsenic species, leading to enhanced adsorption. The initial frequency drop is less pronounced at pH 7 (red curve) compared to pH 3.5, suggesting a relatively lower adsorption capacity at this neutral pH value. This observation aligns with the assertion that optimal adsorption often occurs within the slightly acidic pH range, while at neutral pH values, the adsorption may be reduced due to the presence of different arsenic species or changes in the surface chemistry of the sensor. Notably, the frequency shift curve for pH 11 (green curve) exhibits a distinct behavior. Initially, a slight increase in frequency is observed, indicating a potential desorption or repulsion of species from the sensor's surface. This phenomenon can be attributed to the deprotonation of functional groups at high pH values, leading to electrostatic repulsion between the negatively charged sensor surface and the negatively charged arsenic species present in the solution. Moreover, as the pH level is elevated, the leaching of arsenic becomes apparent, as mentioned in the provided text. This leaching effect results in a decreased rate of adsorption, consequently diminishing the removal capacity of arsenic ions, as visually depicted by the gradual decrease in frequency after the initial increase at pH 11. The observed behavior at high pH can be further expounded upon by considering the augmented presence of sodium ions (Na^+) in the solution, which is attributed to pH adjustments. These sodium ions can compete with the remaining arsenic ions for the available exchangeable sites on the sensor's surface, thereby hindering the adsorption of arsenic ions and contributing to the observed decrease in frequency shift. It is worth noting that the specific shapes and magnitudes of the frequency shift curves can be influenced by various factors, such as the concentration of arsenic ions, the surface chemistry and morphology of the nano-quinazoline manganese complex, the presence of competing ions or interfering species in the solution, and the stability of different arsenic species at varying pH levels [119, 120]. Further investigations, including detailed kinetic studies, surface characterization techniques, computational modeling, and speciation studies, could provide deeper insights into the pH-dependent adsorption mechanisms, the influence of leaching and competing ions, and the underlying intermolecular interactions between the nano-quinazoline manganese complex and arsenic ions at different pH conditions.

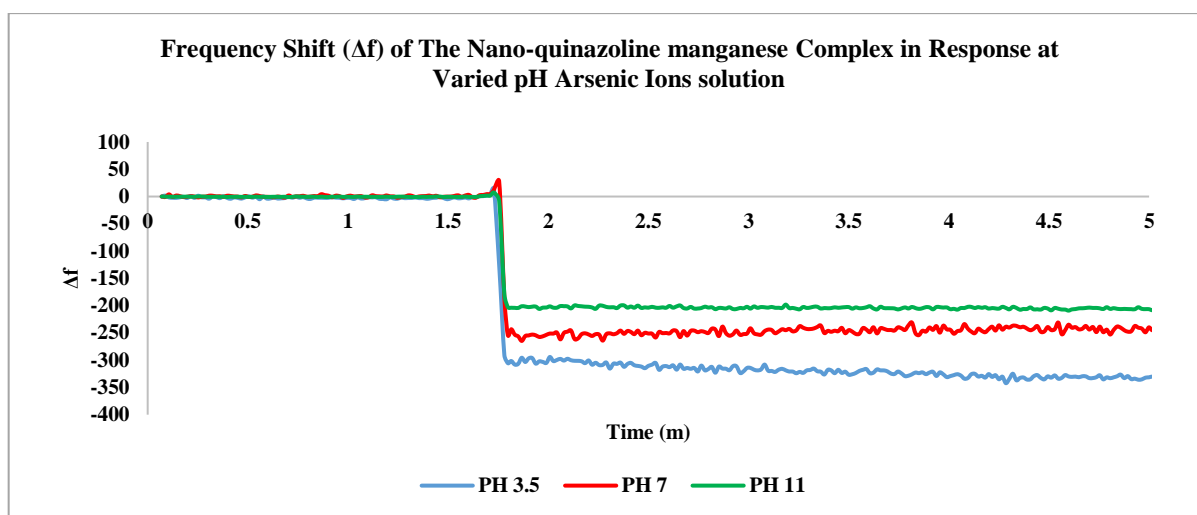


Fig 11. Frequency Shift Response of the Nano-Quinazoline Manganese Complex Sensor for Arsenic Ion Detection at Different pH Levels (3.5, 7, 11).

4. Conclusion

In conclusion, this study presents the successful synthesis, characterization, and application of an innovative quinazoline Schiff base ligand (WMS) and its corresponding mixed-ligand manganese (II) complex, $[\text{Mn}(\text{WMS})(\text{Gly})\text{H}_2\text{O}] \cdot \text{Cl} \cdot \text{H}_2\text{O}$, for arsenic sensing. When integrated into a quartz crystal microbalance (QCM) platform, the complex exhibited remarkable sensing capabilities for detecting arsenic ions. The nano-sized quinazoline manganese complex demonstrated rapid response times, excellent mechanical stability, and consistent performance across varying pH and temperature conditions, highlighting its potential for continuous environmental monitoring of arsenic contamination. Computational investigations employing density functional theory (DFT) and molecular docking simulations provided valuable insights into the complex's structural, electronic, and biological properties. The HOMO-LUMO energy gap analysis suggested enhanced chemical reactivity and stability, while docking studies revealed favorable binding interactions with a cancer-relevant target receptor, corroborating the observed anticancer activity. Furthermore, the nano-quinazoline manganese complex exhibited exceptional colloidal stability, uniform size distribution, and a notable BET surface area, mesoporous structure, and hydrophobic nature. These characteristics contribute to its promising performance as a sensing material for selectively detecting arsenic ions in aqueous environments. Overall, this research highlights the synthesis of novel arsenic-sensing material and its potential applications in continuous environmental monitoring and cancer therapy. The integration of experimental and computational approaches has facilitated a comprehensive understanding of the material's properties and functionality, paving the way for the development of sensitive and selective arsenic sensors and potential therapeutic agents targeting Breast cancer.

References

1. K. Khosravi-Darani, Y. Rehman, I. A. Katsoyiannis, E. Kokkinos, and A. I. Zouboulis, "Arsenic exposure via contaminated water and food sources," *Water*, vol. 14, no. 12, p. 1884, 2022.
2. M. S. Rahaman et al., "Environmental arsenic exposure and its contribution to human diseases, toxicity mechanism and management," *Environ. Pollut.*, vol. 289, p. 117940, 2021.
3. C. R. Tyler and A. M. Allan, "The effects of arsenic exposure on neurological and cognitive dysfunction in human and rodent studies: a review," *Curr. Environ. Heal. reports*, vol. 1, pp. 132–147, 2014.
4. S. Dastgiri et al., "Arsenic exposure, dermatological lesions, hypertension, and chromosomal abnormalities among people in a rural community of northwest Iran," *J. Health. Popul. Nutr.*, vol. 28, no. 1, p. 14, 2010.
5. V. C. Ezeh and T. C. Harrop, "A sensitive and selective fluorescence sensor for the detection of arsenic (III) in organic media," *Inorg. Chem.*, vol. 51, no. 3, pp. 1213–1215, 2012.
6. P. Devi, A. Thakur, R. Y. Lai, S. Saini, R. Jain, and P. Kumar, "Progress in the materials for optical detection of arsenic in water," *TrAC Trends Anal. Chem.*, vol. 110, pp. 97–115, 2019.
7. M. Aljhdali and A. A. El-Sherif, "Synthesis, characterization, molecular modeling and biological activity of mixed ligand complexes of Cu (II), Ni (II) and Co (II) based on 1, 10-phenanthroline and novel thiosemicarbazone," *Inorganica Chim. Acta*, vol. 407, pp. 58–68, 2013.
8. H. M. Helal, A. S. El-Awdan, A. M. Salem, A. T. Abd-Elaziz, Y. A. Moahamed, A. A. El-Sherif, & M. A. G. Mohamed "Synthesis, biological evaluation and molecular modeling of novel series of pyridine derivatives as anticancer, anti-inflammatory and analgesic agents," *Spectrochim. Acta Part A Mol. Biomol. Spectrosc.*, vol. 135, pp. 764–773, 2015.
9. A. A. El-Sherif and T. M. A. Eldebss, "Synthesis, spectral characterization, solution equilibria, in vitro antibacterial and cytotoxic activities of Cu (II), Ni (II), Mn (II), Co (II) and Zn (II) complexes with Schiff base derived from 5-bromosalicylaldehyde and 2-aminomethylthiophene," *Spectrochim. Acta Part A Mol. Biomol. Spectrosc.*, vol. 79, no. 5, pp. 1803–1814, 2011.

10. M. Mansour, F. E.-T. Heikal, and A. El-sherif, "Potentiometric, Thermodynamics, and Modeling Investigates of Binary and Ternary Zn (II) Complexes Prepared from 1-H-Benzimidazole-2-Carboxylic Acid and Some Biologically Active Ligands," Fakiha El-Taib El-sherif, Ahmed, Potentiometric, Thermodyn. Model. Investig. Bin. Ternary Zn Complexes Prep. from.
11. M. S. Mansour, W. H. Mahmoud, and A. A. El-Sherif, "Manganese, Cobalt, and Cadmium Complexes of Quinazoline Schiff Base Ligand and Methionine: Synthesis, Characterization, DFT, Docking studies and biomedical application," Egypt. J. Chem., 2024.
12. X. Liu and J.-R. Hamon, "Recent developments in penta-, hexa- and heptadentate Schiff base ligands and their metal complexes," Coord. Chem. Rev., vol. 389, pp. 94–118, 2019.
13. A. T. A. Karim and A. A. El-Sherif, "Physicochemical studies and biological activity of mixed ligand complexes involving bivalent transition metals with a novel Schiff base and glycine as a representative amino acid," Eur. J. Chem., vol. 5, no. 2, pp. 328–333, 2014.
14. H. Kargar, M. Ashfaq, M. Fallah-Mehrjardi, R. Behjatmanesh-Ardakani, K. S. Munawar, and M. N. Tahir, "Synthesis, crystal structure, spectral characterization, theoretical and computational studies of Ni (II), Cu (II) and Zn (II) complexes incorporating Schiff base ligand derived from 4-(diethylamino) salicylaldehyde," Inorganica Chim. Acta, vol. 536, p. 120878, 2022.
15. A. Singh, H. P. Gogoi, and P. Barman, "Comparative study of palladium (II) complexes bearing tridentate ONS and NNS Schiff base ligands: Synthesis, characterization, DFT calculation, DNA binding, bioactivities, catalytic activity, and molecular docking," Polyhedron, vol. 221, p. 115895, 2022.
16. S. H. Sumrra et al., "Computational investigation of molecular structures, spectroscopic properties, cholinesterase inhibition and antibacterial activities of triazole Schiff bases endowed metal chelates," J. Mol. Struct., vol. 1238, p. 130382, 2021.
17. M. S. Aljahdali and A. A. El-Sherif, "Synthesis and biological evaluation of novel Zn (II) and Cd (II) Schiff base complexes as antimicrobial, antifungal, and antioxidant agents," Bioinorg. Chem. Appl., vol. 2020, pp. 1–17, 2020.
18. A. M. Abu-Dief and I. M. A. Mohamed, "A review on versatile applications of transition metal complexes incorporating Schiff bases," Beni-suef Univ. J. basic Appl. Sci., vol. 4, no. 2, pp. 119–133, 2015.
19. J. M. Mir, Smart Materials of Medicinal and Industrial Relevance. AVID SCIENCE, 2018.
20. F. Arjmand, S. Tabassum, and H. Y. Khan, "Classification of Metal-Based Anticancer Chemotherapeutic Agents," in Advances and Prospects of 3-d Metal-Based Anticancer Drug Candidates, Springer, 2024, pp. 35–71.
21. P. C. Agu et al., "Molecular docking as a tool for the discovery of molecular targets of nutraceuticals in diseases management," Sci. Rep., vol. 13, no. 1, p. 13398, 2023.
22. N. R. Gosu, V. Losetty, and S. Sampath, "Molecular docking studies, structural analysis, biological studies, and synthesis of certain novel Schiff base from benzohydrazide derivate," Phys. Scr., vol. 99, no. 5, p. 55011, 2024.
23. R. M. Ramadan and A. F. H. Noureldeen, "12 Molecular Docking and Drug Design of Schiff Base Metal Complexes," Struct. Biol. Appl. Schiff Base Met. Complexes, p. 221, 2023.
24. M. A. R. Khan et al., "A review on synthesis, characterizations, and applications of Schiff base functionalized nanoparticles," Results Chem., vol. 6, p. 101160, 2023.
25. X. Zhong, Z. Li, R. Shi, L. Yan, Y. Zhu, and H. Li, "Schiff base-modified nanomaterials for ion detection: a review," ACS Appl. Nano Mater., vol. 5, no. 10, pp. 13998–14020, 2022.
26. S. B. Khan et al., "Effect of particle size on the photocatalytic activity and sensing properties of CeO₂ nanoparticles," Int. J. Electrochem. Sci., vol. 8, no. 5, pp. 7284–7297, 2013.
27. N. Sharma, H. Ojha, A. Bharadwaj, D. P. Pathak, and R. K. Sharma, "Preparation and catalytic applications of nanomaterials: a review," Rsc Adv., vol. 5, no. 66, pp. 53381–53403, 2015.
28. S. Hannah, E. Blair, and D. K. Corrigan, "Developments in microscale and nanoscale sensors for biomedical sensing," Curr. Opin. Electrochem., vol. 23, pp. 7–15, 2020.
29. R. Antony, T. Arun, and S. T. D. Manickam, "A review on applications of chitosan-based Schiff bases," Int. J. Biol. Macromol., vol. 129, pp. 615–633, 2019.
30. S. Goyal, U. Bansal, and S. Agrawal, "BIOLOGICALLY ACTIVE SCHIFF BASE NANOPARTICLES: A REVIEW," Eur. J. Biomed., vol. 8, no. 9, pp. 244–252, 2021.
31. W. H. Mahmoud, A. A. Fayek, A. Taha, and A. A. El-Sherif, "Synthesis, textural and thermal properties of Nano super hydrophobic copper complex as QCM based dye sensor," Egypt. J. Chem., vol. 67, no. 4, pp. 485–494, 2024.
32. N. Bibi, I. T. Awan, and A. T. Awan, "New Adsorption-Based Biosensors for Cancer Detections and Role of Nanomedicine in Its Prognosis and Inhibition," Essentials Cancer Genomic, Comput. Approaches Precis. Med., pp. 107–140, 2020.
33. W. H. Mahmoud, A. A. Fayek, and A. A. El-Sherif, "Chromium complex nanoparticles sensor for arsenic detection using QCM technique," Egypt. J. Chem., vol. 67, no. 5, pp. 463–470, 2024.
34. W. H. Mahmoud and A. A. El-Sherif, "Design and characterization of Nano cobalt complex as low limit detection qcm sensor for cadmium ions," Egypt. J. Chem., vol. 67, no. 5, pp. 471–478, 2024.
35. M. Mazumdar, D. Fournier, D.-W. Zhu, C. Cadot, D. Poirier, and S.-X. Lin, "Binary and ternary crystal structure analyses of a novel inhibitor with 17 β -HSD type 1: a lead compound for breast cancer therapy," Biochem. J., vol. 424, no. 3, pp. 357–366, 2009.
36. R. Schrawat et al., "In silico design of novel bioactive molecules to treat breast cancer with chlorogenic acid derivatives: a computational and SAR approach," Front. Pharmacol., vol. 14, no. December, 2023.

37. M. S. A. Mansour, A. A. El-Sherif, W. H. Mahmoud, and Abeer Taha, "QCM-Based Nano Schiff base Quinazoline-methionine hybrid ligand complex with Cobalt (II) as a Fast Response Nanosensor for instantaneous Monitoring water pollutant Pb (II) Ions," *Egypt. J. Chem.*, 2024.
38. X. Wu and A. K. Ray, "Density-functional study of water adsorption on the PuO₂ (110) surface," *Phys. Rev. B*, vol. 65, no. 8, p. 85403, 2002.
39. W. J. Hehre, "Ab initio molecular orbital theory," *Acc. Chem. Res.*, vol. 9, no. 11, pp. 399–406, 1976.
40. P. Pilot, "7.5. Accelrys Software Inc.: San Diego, CA, USA."
41. A. Matveev, M. Staufer, M. Mayer, and N. Rösch, "Density functional study of small molecules and transition-metal carbonyls using revised PBE functionals," *Int. J. Quantum Chem.*, vol. 75, no. 4-5, pp. 863–873, 1999.
42. Y. Gu and M. Li, "Molecular modeling," in *Handbook of Benzoxazine Resins*, Elsevier, 2011, pp. 103–110.
43. A. D. Studio, "1.7 Accelrys Software Inc," San Diego, CA, USA, 2006.
44. B. Hammer, L. B. Hansen, and J. K. Nørskov, "Improved adsorption energetics within density-functional theory using revised Perdew-Burke-Ernzerhof functionals," *Phys. Rev. B*, vol. 59, no. 11, p. 7413, 1999.
45. A. Bauer, W. M. M. Kirby, and J. C. Sherris, "turck, Turck M. Antibiotic susceptibility testing by a standardized single disk method," *Am. J. Clin. Pathol.*, vol. 45, no. 4, p. 493, 1966.
46. A. A. El-Sherif, "Mixed ligand complex formation reactions and equilibrium studies of Cu (II) with bidentate heterocyclic alcohol (N, O) and some bio-relevant ligands," *J. Solution Chem.*, vol. 39, pp. 131–150, 2010.
47. A. Boulekbache et al., "Comparison of daptomycin and glycopeptide efficacy and safety for the treatment of Gram-positive infections: a systematic review and meta-analysis," *J. Antimicrob. Chemother.*, vol. 79, no. 4, pp. 712–721, Apr. 2024.
48. C. Li, Z. Ouyang, and J. Liu, "Bacterial growth and cultivation," in *Molecular Medical Microbiology*, Elsevier, 2024, pp. 155–175.
49. D. A. S. et al Michael C. Alley, "Feasibility of drug screening with panels of human tumor cell lines.pdf," *Cancer Res*, vol. 48. pp. 589–601, 1988.
50. A. A. van de Loosdrecht, R. H. J. Beelen, G. J. Ossenkoppele, M. G. Broekhoven, and M. M. A. C. Langenhuijsen, "A tetrazolium-based colorimetric MTT assay to quantitate human monocyte mediated cytotoxicity against leukemic cells from cell lines and patients with acute myeloid leukemia," *J. Immunol. Methods*, vol. 174, no. 1–2, pp. 311–320, Sep. 1994.
51. P. Pandey, V. Verma, G. Gautam, N. Kumari, S. K. Dhar, and S. Gourinath, "Targeting the β -clamp in *Helicobacter pylori* with FDA-approved drugs reveals micromolar inhibition by diflunisal," *FEBS Lett.*, vol. 591, no. 15, pp. 2311–2322, 2017.
52. Available: <https://www.bioline.com/qsense>.
53. W. Al-Gethami, D. Alhashmialameer, N. Al-Qasbi, S. H. Ismail, and A. H. Sadek, "Design of a Novel Nanosensors Based on Green Synthesized CoFe₂O₄/Ca-Alginate Nanocomposite-Coated QCM for Rapid Detection of Pb (II) Ions," *Nanomaterials*, vol. 12, no. 20, p. 3620, 2022.
54. Q. Zhang et al., "QCM-nanomagnetic beads biosensor for lead ion detection," *Analyst*, vol. 143, no. 2, pp. 549–554, 2018.
55. Q. Chen, S. Xu, Q. Liu, J. Masliyah, and Z. Xu, "QCM-D study of nanoparticle interactions," *Adv. Colloid Interface Sci.*, vol. 233, pp. 94–114, 2016.
56. C. Song, Z. Ma, C. Li, H. Zhang, Z. Zhu, and J. Wang, "Application of Heat-Enhancement for Improving the Sensitivity of Quartz Crystal Microbalance," *Biosensors*, vol. 12, no. 8, p. 643, 2022.
57. J. J. Hamon, A. Striolo, and B. P. Grady, "Observing the Effects of Temperature and Surface Roughness on Cetyltrimethylammonium Bromide Adsorption Using a Quartz-Crystal Microbalance with Dissipation Monitoring," *J. Surfactants Deterg.*, vol. 22, no. 5, pp. 1201–1212, 2019.
58. W. H. Mahmoud, A. A. Fayek, A. Taha, and A. A. El-Sherif, "Synthesis, textural and thermal properties of Nano super hydrophobic copper complex as QCM based dye sensor," *Egypt. J. Chem.*, 2023.
59. W. Rehman, R. Yasmeen, F. Rahim, and M. Waseem, "CY, Guo, Z. Hassa, U. Rashid, K," *J Photochem. Photobiol., B Biol.*, vol. 164, p. 65, 2016.
60. E. Ghasemi Gorji, N. Monadi, and M. Mohseni, "Synthesis, characterization and antibacterial activities of Mo (VI) and Cu (II) complexes derived from tridentate ONO Schiff base ligands," *Appl. Chem.*, vol. 11, no. 41, pp. 119–128, 2016.
61. S. A. Sadeek, A. El-Hamid, S. Mohamed, and N. Rashid, "Spectroscopic characterization and XRD of some new metal complexes with dithranol in presence of 8-hydroxyquinoline," *Egypt. J. Chem.*, vol. 63, no. 3, pp. 939–951, 2020.
62. H. F. Abd El-Halim, M. M. Omar, and M. N. Anwar, "Preparation, characterization, antimicrobial and anticancer activities of Schiff base mixed ligand complexes," *J. Therm. Anal. Calorim.*, vol. 130, pp. 1069–1083, 2017.
63. K. Mohammadi, S. S. Azad, and A. Amoozegar, "New tetradentate Schiff bases of 2-amino-3, 5-dibromobenzaldehyde with aliphatic diamines and their metal complexes: Synthesis, characterization and thermal stability," *Spectrochim. Acta Part A Mol. Biomol. Spectrosc.*, vol. 146, pp. 221–227, 2015.
64. M. Aljahdali and A. A. El-Sherif, "Synthesis, characterization, molecular modeling and biological activity of mixed ligand complexes of Cu (II), Ni (II) and Co (II) based on 1, 10-phenanthroline and novel thiosemicarbazone," *Inorganica Chim. Acta*, vol. 407, pp. 58–68, 2013.
65. A. A. El-Sherif, "Synthesis, spectroscopic characterization and biological activity on newly synthesized copper (II) and nickel (II) complexes incorporating bidentate oxygen–nitrogen hydrazone ligands," *Inorganica Chim. Acta*, vol. 362, no. 14, pp. 4991–5000, 2009.

66. A. A. El-Sherif, M. S. Aljhdali, A. T. AbedelKarim, and M. M. Ahmed, "Physicochemical Studies and Biological Activity of Mixed Ligand Complexes Involving Bivalent Transition Metals, 2-Aminomethylthiophenyl-4-Bromosalicylaldehyde Schiff Base and Glycine" Vol.7 No.7, 2015.
67. M. Anu, L. Prabha, G. Banukarhi, P. R. Kanjana, and K. Rajeswari, "UV-visible, IR and NMR spectra on Copper (II) Schiff base Complex," Int. J. Institutional Pharm. Life Sci., vol. 3, no. 6, pp. 23–32, 2013.
68. B. K. Singh, H. K. Rajour, and A. Prakash, "Synthesis, characterization and biological activity of transition metal complexes with Schiff bases derived from 2-nitrobenzaldehyde with glycine and methionine," Spectrochim. Acta Part A Mol. Biomol. Spectrosc., vol. 94, pp. 143–151, 2012.
69. A. Kumar et al., "In vitro Anti-microbial, DNA-binding. In silico Pharmacokinetics and Molecular Docking Studies of Schiff-based Cu(II), Zn(II) and Pd(II) Complexes," J. Mol. Struct., p. 138695, May 2024.
70. A. A. Hamed, C. M. Sharaby, M. F. Amine, Y. A. Ammar, and A. A. El-Sherif, "In Vitro Anticancer and Antibacterial Assessment of Novel Metal Complexes of 1,3-di-[P-Toly]-2,4-di-[9H-Purin-6-YI]-2,4-Dichlorocyclodiphosph(V)Azane," Egypt. J. Chem., vol. 65, no. 13, pp. 843–857, 2022.
71. S. İlhan, "Synthesis and spectral studies of new macrocyclic Schiff base Cu (II), Ni (II), Cd (II), Zn (II), Pb (II), and La (III) complexes containing pyridine head unit," Russ. J. Coord. Chem., vol. 35, no. 5, pp. 347–351, 2009.
72. A. A. Abou-Hussein and W. Linert, "Synthesis, spectroscopic, coordination and biological activities of some organometallic complexes derived from thio-Schiff base ligands," Spectrochim. Acta Part A Mol. Biomol. Spectrosc., vol. 117, pp. 763–771, 2014.
73. M. A. Arafath, F. Adam, M. R. Razali, L. E. A. Hassan, M. B. K. Ahamed, and A. M. S. A. Majid, "Synthesis, characterization and anticancer studies of Ni (II), Pd (II) and Pt (II) complexes with Schiff base derived from N-methylhydrazinecarbothioamide and 2-hydroxy-5-methoxy-3-nitrobenzaldehyde," J. Mol. Struct., vol. 1130, pp. 791–798, 2017.
74. G. L. French, "Bactericidal agents in the treatment of MRSA infections—the potential role of daptomycin," J. Antimicrob. Chemother., vol. 58, no. 6, pp. 1107–1117, 2006.
75. P. Skehan et al., "New colorimetric cytotoxicity assay for anticancer-drug screening," JNCI J. Natl. Cancer Inst., vol. 82, no. 13, pp. 1107–1112, 1990.
76. H. A. El-Boraey and A. A. S. El-Din, "Transition metal complexes of a new 15-membered [N5] penta-azamacrocyclic ligand with their spectral and anticancer studies," Spectrochim. Acta Part A Mol. Biomol. Spectrosc., vol. 132, pp. 663–671, 2014.
77. T. Mosmann, "Rapid colorimetric assay for cellular growth and survival: application to proliferation and cytotoxicity assays," J. Immunol. Methods, vol. 65, no. 1–2, pp. 55–63, 1983.
78. P. Tyagi, M. Tyagi, S. Agrawal, S. Chandra, H. Ojha, and M. Pathak, "Synthesis, characterization of 1,2,4-triazole Schiff base derived 3d-metal complexes: Induces cytotoxicity in HepG2, MCF-7 cell line, BSA binding fluorescence and DFT study," Spectrochim. Acta - Part A Mol. Biomol. Spectrosc., vol. 171, pp. 246–257, 2017, doi: 10.1016/j.saa.2016.08.008.
79. A. A. El-Sherif, A. Fetoh, Y. K. Abdulhamed, and G. M. A. El-Reash, "Synthesis, structural characterization, DFT studies and biological activity of Cu (II) and Ni (II) complexes of novel hydrazone," Inorganica Chim. Acta, vol. 480, pp. 1–15, 2018.
80. H. L. Singh, J. B. Singh, and S. Bhanuka, "Synthesis, spectral, DFT, and antimicrobial studies of tin(II) and lead(II) complexes with semicarbazone and thiosemicarbazones derived from (2-hydroxyphenyl)(pyrrolidin-1-yl)methanone," J. Coord. Chem., vol. 69, no. 2, pp. 343–353, 2016.
81. A. A. El-Sherif, M. M. Shoukry, and M. M. A. Abd-Elgawad, "Synthesis, characterization, biological activity and equilibrium studies of metal(II) ion complexes with tridentate hydrazone ligand derived from hydralazine," Spectrochim. Acta Part A Mol. Biomol. Spectrosc., vol. 98, pp. 307–321, Dec. 2012.
82. V. Sunil Kumar et al., "Anti-fibrinolytic activity, electron delocalization, vibrational spectra, drug - likeness properties and bio-activity studies on Anagrelide," Results Chem., vol. 7, no. February, p. 101379, 2024.
83. S. A. Sadeek, S. M. Abd El-Hamid, A. A. Mohamed, W. A. Zordok, and H. A. El-Sayed, "Spectroscopic characterization, thermogravimetry, density functional theory and biological studies of some mixed-ligand complexes of meloxicam and 2, 2'-bipyridine with some transition metals," Appl. Organomet. Chem., vol. 33, no. 5, p. e4889, 2019.
84. M. A. El-Bindary and A. A. El-Bindary, "Synthesis, characterization, DNA binding, and biological action of dimedone arylhydrazone chelates," Appl. Organomet. Chem., vol. 36, no. 4, p. e6576, 2022.
85. M. A. El-Ghamry, F. M. Elzawawi, A. A. A. Aziz, K. M. Nassir, and S. M. Abu-El-Wafa, "New Schiff base ligand and its novel Cr (III), Mn (II), Co (II), Ni (II), Cu (II), Zn (II) complexes: Spectral investigation, biological applications, and semiconducting properties," Sci. Rep., vol. 12, no. 1, p. 17942, 2022.
86. M. S. Masoud, G. A. Yacout, B. A. Abd-El-Khalek, and A. M. Ramadan, "Synthesis, Physicochemical Characterization, Biological Assessment, and Molecular Docking Study of Some Metal Complexes of Alloxan and Ninhydrin as Alterdentate Ligands," J. Inorg. Organomet. Polym. Mater., vol. 33, no. 8, pp. 2252–2269, 2023.
87. A. L. Patterson, "The Scherrer formula for X-ray particle size determination," Phys. Rev., vol. 56, no. 10, p. 978, 1939.
88. S. Mourdikoudis, R. M. Pallares, and N. T. K. Thanh, "Characterization techniques for nanoparticles: comparison and complementarity upon studying nanoparticle properties," Nanoscale, vol. 10, no. 27, pp. 12871–12934, 2018.
89. L. Angeloni, D. Passeri, P. G. Schiavi, F. Pagnanelli, and M. Rossi, "Magnetic force microscopy characterization of cobalt nanoparticles: A preliminary study," in AIP Conference Proceedings, AIP Publishing, 2020.

90. C. M. Hoo, N. Starostin, P. West, and M. L. Mecartney, "A comparison of atomic force microscopy (AFM) and dynamic light scattering (DLS) methods to characterize nanoparticle size distributions," *J. Nanoparticle Res.*, vol. 10, no. SUPPL. 1, pp. 89–96, 2008.
91. D. Chicea, "Nanoparticles and nanoparticle aggregates sizing by DLS and AFM," *Optoelectron. Adv. Mater. Rapid Commun.*, vol. 4, no. 9, pp. 1310–1315, 2010.
92. S. Bhattacharjee, "DLS and zeta potential – What they are and what they are not?," *J. Control. Release*, vol. 235, pp. 337–351, Aug. 2016.
93. F. Babick, "Dynamic light scattering (DLS)," in *Characterization of Nanoparticles*, Elsevier, 2020, pp. 137–172.
94. G. V. Lowry et al., "Guidance to improve the scientific value of zeta-potential measurements in nanoEHS," *Environ. Sci. Nano*, vol. 3, no. 5, pp. 953–965, 2016.
95. H. Takeuchi, H. Yamamoto, and Y. Kawashima, "Mucoadhesive nanoparticulate systems for peptide drug delivery," *Adv. Drug Deliv. Rev.*, vol. 47, no. 1, pp. 39–54, 2001.
96. K. Fernández, J. Aburto, C. von Plessing, M. Rockel, and E. Aspé, "Factorial design optimization and characterization of poly-lactic acid (PLA) nanoparticle formation for the delivery of grape extracts," *Food Chem.*, vol. 207, pp. 75–85, 2016.
97. M. Zhou, Z. Wei, H. Qiao, L. Zhu, H. Yang, and T. Xia, "Particle size and pore structure characterization of silver nanoparticles prepared by confined arc plasma," *J. Nanomater.*, vol. 2009, 2009.
98. N. Hwang and A. R. Barron, "BET surface area analysis of nanoparticles," *connexions Proj.*, pp. 1–11, 2011.
99. J. W. M. Osterrieth et al., "How reproducible are surface areas calculated from the BET equation?," *Adv. Mater.*, vol. 34, no. 27, p. 2201502, 2022.
100. R. Bardestani, G. S. Patience, and S. Kaliaguine, "Experimental methods in chemical engineering: specific surface area and pore size distribution measurements—BET, BJH, and DFT," *Can. J. Chem. Eng.*, vol. 97, no. 11, pp. 2781–2791, 2019.
101. N. Gao and Y. Yan, "Characterisation of surface wettability based on nanoparticles," *Nanoscale*, vol. 4, no. 7, pp. 2202–2218, 2012.
102. X. Zhang, H. Liu, and L. Jiang, "Wettability and applications of nanochannels," *Adv. Mater.*, vol. 31, no. 5, p. 1804508, 2019.
103. Z. Wang, M. Elimelech, and S. Lin, "Environmental applications of interfacial materials with special wettability," *Environ. Sci. Technol.*, vol. 50, no. 5, pp. 2132–2150, 2016.
104. M. Tucci, "Microbial electrochemical sensors for freshwater and wastewater monitoring," 2020.
105. M. Ismail et al., "Pollution, toxicity and carcinogenicity of organic dyes and their catalytic bio-remediation," *Curr. Pharm. Des.*, vol. 25, no. 34, pp. 3645–3663, 2019.
106. N. Alanazi, M. Almutairi, and A. N. Alodhayb, "A review of quartz crystal microbalance for chemical and biological sensing applications," *Sens. Imaging*, vol. 24, no. 1, p. 10, 2023.
107. S. Kumar, P. Singh, and S. K. Verma, "Selection of Highly Specific DNA Aptamer for the Development of QCM-Based Arsenic Sensor," *ChemBioChem*, vol. 24, no. 24, p. e202300585, 2023.
108. H. J. Park and S. S. Lee, "Strategic Approaches for Highly Selective and Sensitive Detection of Hg²⁺ Ion Using Mass Sensitive Sensors," *Anal. Sci.*, vol. 35, no. 8, pp. 883–888, 2019.
109. C. Li, A. E. Başaran, and J. F. Tyson, "Determination of inorganic arsenic in water by a quartz crystal microbalance," *Anal. methods*, vol. 5, no. 22, pp. 6286–6291, 2013.
110. Z. Guo et al., "Detection of heavy metals in food and agricultural products by surface-enhanced Raman spectroscopy," *Food Rev. Int.*, vol. 39, no. 3, pp. 1440–1461, 2023.
111. A. Singh et al., "Recent advances in electrochemical biosensors: Applications, challenges, and future scope," *Biosensors*, vol. 11, no. 9, p. 336, 2021.
112. N. Al-Qasbi, W. Al-Gethami, D. Alhashmialameer, S. H. Ismail, and A. H. Sadek, "Evaluation of Green-Synthesized Cuprospinel Nanoparticles as a Nanosensor for Detection of Low-Concentration Cd(II) Ion in the Aqueous Solutions by the Quartz Crystal Microbalance Method," *Materials (Basel)*, vol. 15, no. 18, 2022.
113. L. Wang, "Metal-organic frameworks for QCM-based gas sensors: A review," *Sensors Actuators A Phys.*, vol. 307, p. 111984, 2020.
114. S. M. M. Hizam, A. M. Al-Dhahebi, and M. S. Mohamed Saheed, "Recent advances in graphene-based nanocomposites for ammonia detection," *Polymers (Basel)*, vol. 14, no. 23, p. 5125, 2022.
115. Q. Yao, J. Xie, J. Liu, H. Kang, and Y. Liu, "Adsorption of lead ions using a modified lignin hydrogel," *J. Polym. Res.*, vol. 21, pp. 1–16, 2014.
116. N. A. A. Qasem, R. H. Mohammed, and D. U. Lawal, "Removal of heavy metal ions from wastewater: A comprehensive and critical review," *Npj Clean Water*, vol. 4, no. 1, p. 36, 2021.
117. S. N. A. Mustaffa et al., "Sensing mechanism of an optimized room temperature optical hydrogen gas sensor made of zinc oxide thin films," *J. Mater. Res. Technol.*, vol. 9, no. 5, pp. 10624–10634, 2020.
118. D. R. Boverhof and R. M. David, "Nanomaterial characterization: considerations and needs for hazard assessment and safety evaluation," *Anal. Bioanal. Chem.*, vol. 396, pp. 953–961, 2010.
119. X. Yang et al., "Surface functional groups of carbon-based adsorbents and their roles in the removal of heavy metals from aqueous solutions: a critical review," *Chem. Eng. J.*, vol. 366, pp. 608–621, 2019.
120. M. Onditi, A. A. Adelodun, E. O. Changamu, and J. C. Ngila, "Removal of Pb²⁺ and Cd²⁺ from drinking water using polysaccharide extract isolated from cactus pads (*Opuntia ficus indica*)," *J. Appl. Polym. Sci.*, vol. 133, no. 38, 2016.